A Numerical Investigation into the Impact of Micromechanics Models on the Stiffness Parameters of Cross-ply Laminates

By

Darya Forooghi

A Thesis submitted to the
Faculty of Graduate and Postdoctoral Studies
of the University of Manitoba
in partial fulfilment of the requirements of the degree of
Master of Science

Department of Mechanical Engineering
University of Manitoba
Winnipeg

Abstract

Laminate plate and shell structures with symmetric cross-ply configurations are widely used due to their high stiffness-to-weight ratio. However, conventional lamination theories rely on simplifying assumptions that may introduce inaccuracies, and experimental data is often limited and expensive to obtain. Therefore, having a reliable and accurate numerical model as a reference is valuable for evaluating and improving the analytical approach.

This study evaluates the predictive capability of lamination theories by integrating multiple micromechanics models with First-Order Shear Deformation Theory (FSDT), and comparing the results against voxel-based finite element modeling (VB-FEM), which serves as a high-fidelity numerical reference. A range of models—including Voigt–Reuss, Chamis, Halpin–Tsai and its modified form, Generalized Self-Consistent, Mori–Tanaka, Bridging, and two iterative isotropized formulations—are assessed for unidirectional laminae. The most accurate micromechanics models are then used in combination with FSDT to assess the stiffness predictions for cross-ply laminates. Predictions are evaluated across a wide range of fiber volume fractions, from approximately 10% to 70%.

Comparison reveals that while all models predict the longitudinal modulus accurately, significant deviations arise in predicting transverse and shear properties. The Bridging model consistently yields the closest agreement with VB-FEM across all five elastic constants, maintaining accuracy even at high volume fractions where the modified Halpin–Tsai model begins to fail. Discrepancies in micromechanics-based lamina properties propagate to laminate-level stiffness predictions, highlighting the critical role of model selection. These findings establish VB-FEM as a valuable tool for validating analytical models and guide improved modeling strategies for laminated composite design.

Acknowledgments

First, I would like to thank my supervisor, Dr. Yuhua Luo, for his support and guidance throughout my master's journey. At the very beginning of the program, when I was unsure of what topic to pursue for my research, he shared a perspective that stayed with me: *what truly matters is not the subject you choose, but learning how to approach and solve a problem.* That advice gave me clarity and helped me shift my focus toward building the skills and mindset needed to tackle challenges thoughtfully and effectively—something I'll carry with me far beyond this degree.

I would also like to thank Dr. Guo-Zhen Zhu and Dr. Igor Telichev, whose courses introduced me to new and interesting areas of study. I truly enjoyed learning about the world of electron microscopy of materials with Dr. Zhu and building a valuable understanding of fracture mechanics with Dr. Telichev. Their teaching sparked my curiosity and gave me a solid foundation in topics I am now deeply interested in.

Lastly, I'm grateful to my lab mates for creating a supportive and collaborative environment. Their thoughtful suggestions and friendly conversations made a big difference, especially during the more challenging times of this program.

Dedication

To everyone who taught me a lesson along the way.

Contents

List of Tables

List of Figures

List of Abbreviations

APDL	ANSYS Parametric Design Language
Br	Bridging
CLT	Classical Lamination Theory
FEA	Finite Element Analysis
FEM	Finite Element Method
FSDT	First-Order Shear Deformation Theory
GB-FEM	Geometry-Based Finite Element Modeling
GSCM	Generalized Self-Consistent Method
HT	Halpin-Tsai
HTm	Halpin-Tsai modified
HS	Hashin–Shtrikman
Iter-Iso-HS	Iterative Isotropized Hashin–Shtrikman
Iter-Iso-VR	Iterative Isotropized Voigt–Reuss
MT	Mori–Tanaka
RVE	Representative Volume Element
VB-FEM	Voxel-Based Finite Element Modeling
VR	Voigt–Reuss

List of Symbols

A_{ij}	In-plane stiffness matrix
B_{ij}	Coupling matrix
D_{ij}	Bending stiffness matrix
E_1	Longitudinal elastic modulus
E_2	Transversal elastic modulus
E_1^f	Fiber longitudinal elastic modulus
E_2^f	Fiber transversal elastic modulus
E^m	Matrix elastic modulus
$E_U^{(i)}$	The upper bound of elastic modulus in i^{th} iteration
$E_L^{(i)}$	The lower bound of elastic modulus in i^{th} iteration
E_x^f, E_y^f	Effective flexural Young's moduli of laminate
f_1, f_2	Phase volume fraction
G_{12}	In-plane shear modulus
G_{23}	Out-of-plane shear modulus
G_{12}^f	Fiber in-plane shear modulus
G_{23}^f	Fiber out-of-plane shear modulus
G^m	Matrix shear modulus
$G_U^{(i)}$	The upper bound of shear modulus in i-th iteration
$G_L^{(i)}$	The lower bound of shear modulus in i-th iteration

H_{ij}	Transverse shear stiffness matrix
K_{23}	Out-of-plane bulk modulus
K_{23}^{f}	Fiber out-of-plane bulk modulus
K^{m}	Matrix bulk modulus
$K_{U}^{(i)}$	The upper bound of bulk modulus in i-th iteration
$K_{L}^{(i)}$	The lower bound of bulk modulus in i-th iteration
Q^{*}	Stiffness matrix derived from S^{*}
$(\overline{Q}_{ij})_{k}$	Transformed reduced stiffness matrix of k-th lamina into the global coordinate system of the laminate
S	Compliance matrix
S^{*}	Remaining two equations to complete the compliance matric
t	Thickness of laminate
$T(\theta)$	Transformation matrix
t_{k}	Thickness of k-th lamina
ν_{12}	In-plane Poisson's ratio
ν_{12}^{f}	Fiber in-plane Poisson's ratio
ν^{m}	Matrix Poisson's ratio
V_{f}	Fiber volume fraction
$\bar{z}_{k}$	Coordinate of the middle surface of the k-th lamina
σ	Normal stress
ε	Normal strain
τ	Shear stress

γ Shear strain

θ Fiber orientation angle

Chapter 1

Introduction

1.1 Background and Motivation

Industries increasingly employ laminate plate/shell structures due to their superior properties, such as high stiffness-to-weight ratios, durability, resistance to corrosion, and design flexibility [1–3]. These materials are now common in applications ranging from aerospace, marine, transportation, and construction. The advantages they offer over traditional materials and the widespread use make them an interesting area for research and development.

Given their extensive use in critical applications, accurately predicting the mechanical behavior of laminate composites is important for reliable design and performance. There are three primary methods to achieve this: analytical, numerical, and experimental. Given the multiple variables involved in designing laminates such as fiber orientation , material properties, volume fraction [3], and fiber distribution [4], analytical formulas are preferred due to their computational efficiency.

The analytical approach operates at two levels: macroscale and microscale. In macroscale analysis, laminate plate/shell theories [5–7] are used to predict the laminate stiffness parameters based on the properties and stacking sequence of each lamina. In microscale analysis, micromechanics models are used to predict the properties of individual laminae, which are typically modeled as transversely isotropic unidirectional fiber composites characterized by five independent elastic constants.

Although analytical formulas are the most efficient, their accuracy differs in different situations, especially with high volume fractions of fibers and large differences between phase properties. For models with empirical parameters, the prediction accuracy of elastic properties is sensitive to the selection of these parameters, and curve fitting may be required to improve accuracy across different conditions. Huang et al [8] and Wang et al [9] investigated the sensitivity of elastic properties prediction to the selection of bridging parameters, concluding that it can be significant for composites with large differences between phase properties.

Moreover, the stiffness parameters of a laminate depend on all five elastic properties of the lamina. However, most micromechanical models only focus on predicting some of these properties, and their accuracy is not consistent across all five properties, as investigated by [10–12]. Although most models accurately predict the longitudinal Young's modulus and Poisson's ratio, there is a lack of accuracy in the prediction of transverse Young's modulus and shear moduli.

Therefore, analytical predictions alone are insufficient, and validation through numerical or experimental data is necessary. Though experimental data are the most reliable, they are cost and time intensive. Due to the large number of design parameters in laminate systems, there is a lack of experimental data to validate analytical predictions, particularly for laminate composites. Existing experimental studies on laminae and laminates typically report only the Young's modulus and often omit the full set of elastic properties needed for complete stiffness characterization.

Given these limitations, numerical simulations are a suitable alternative for validating analytical predictions. They can provide estimates of all required elastic constants and help assess the accuracy of analytical models, especially when experimental data are limited or incomplete.

1.2 Objectives of the Study

Despite the extensive literature on micromechanics models and laminate theories, few studies have systematically compared a broad spectrum of classical, empirical, and recently proposed micromechanics models against high-fidelity voxel-based finite element modeling (VB-FEM). This thesis addresses that gap by evaluating the performance of analytical approaches in predicting the stiffness of symmetric cross-ply laminated composite structures. The focus is on assessing how the accuracy of lamina property predictions—particularly for transverse and shear moduli—affects the overall stiffness predictions when these models are integrated with First-Order Shear Deformation Theory (FSDT). Results from analytical models are compared against a high-fidelity numerical reference and available experimental data.

To achieve this, the following specific objectives are addressed:

1. To develop a voxel-based finite element model (VB-FEM) that provides accurate numerical predictions for the elastic properties of both unidirectional laminae and cross-

ply laminates across a broad range of fiber volume fractions (approximately 10% to 70%).

2. To evaluate a range of micromechanics models—including Voigt–Reuss, Chamis, Halpin–Tsai and its modified form, Generalized Self-Consistent, Mori–Tanaka, Bridging, and two iterative isotropized formulations—in predicting the five independent elastic constants of unidirectional fiber-reinforced laminae, using results from the developed VB-FEM model and available experimental data as references for validation.
3. To integrate the micromechanics-based lamina properties into FSDT and assess the resulting laminate-level stiffness predictions.
4. To compare the predictions obtained from FSDT-micromechanics combinations with the results from the developed VB-FEM model and, where available, experimental data from the literature.
5. To highlight how discrepancies in micromechanics-level predictions affect laminate-level results.

1.3 Scope of the Thesis

This thesis focuses on the elastic stiffness prediction of laminated composite structures composed of unidirectional fiber-reinforced laminae arranged in symmetric cross-ply configurations. The study is limited to linear elastic behavior under small deformations and does not address damage, failure, or environmental effects such as temperature or moisture.

The laminate configuration evaluated in this work is limited to a single symmetric cross-ply layup: [90/90/0/0/90/90]. While only one stacking sequence is analyzed in detail, the developed numerical framework and analytical methodology can be extended to other symmetric cross-ply configurations with minimal modifications.

The research includes a selected set of micromechanics models—both classical and recently proposed—including Voigt–Reuss, Chamis, Halpin–Tsai, Bridging, and two iterative isotropized formulations. More complex or rigorous micromechanics models, such as those based on variational bounds or probabilistic representations of microstructure, are outside the scope of this work but are acknowledged as directions for future study.

Fiber volume fractions are varied from approximately 10% to 70% to investigate the impact of fiber volume fraction on stiffness predictions at both the lamina and laminate levels.

Additionally, limited experimental data are used as reference for validation where available, highlighting the need for accurate numerical modeling in the absence of complete experimental datasets.

1.4 Structure of the Thesis

This thesis is organized into five chapters, each addressing a specific aspect of the research:

Chapter 1: Introduction

Provides background on composite materials, states the motivation and objectives of the study, and outlines the scope and structure of the thesis.

Chapter 2: Literature Review

Reviews fundamental concepts related to composite materials, laminate plate/shell theories, and micromechanics models. It also provides a review of experimental methods—both destructive and non-destructive—used to characterize the stiffness properties of unidirectional laminae and laminate composites. Finally, it highlights the advantages of finite element analysis, particularly voxel-based FEM, and identifies the research gap addressed in this thesis.

Chapter 3: Methodology

Provides the equations for the micromechanics models selected for predicting unidirectional lamina properties and describes their integration with First-Order Shear Deformation Theory (FSDT) to predict laminate stiffness. It then details the implementation of voxel-based finite element modeling (VB-FEM) for both unidirectional and laminate composites, followed by an overview of the experimental cases used for validation.

Chapter 4: Results and Discussion

Presents the numerical results for unidirectional and laminate composites. It compares different micromechanics models against FEM and experimental data and discusses the performance and limitations of each model in predicting various stiffness parameters.

Chapter 5: Conclusion and Future Work

Summarizes the main findings and contributions of the research, discusses limitations, and proposes directions for future studies.

Chapter 2

Literature Review

2.1 Overview of Composite Materials and Laminated Structures

Composites are combinations of two or more materials having superior properties to the individual substances. In continuous fiber composites, long fibers are distributed in a binder material called matrix. Long fibers exhibit significantly greater stiffness and strength compared to their bulk form because fibers have a more ordered structure, with crystals aligned along their length and fewer structural flaws [13–15]. The matrix material is used to bond these fibers, forming a structure that can carry loads. This material supports fibers, protects them from environmental degradation such as chemicals and moisture, and transfers stress between them [16].

A lamina is the basic building block of a laminate, and in a unidirectional fiber lamina, fibers are aligned in the same direction [13]. This structure is strong and stiff along the fiber direction but weaker in other directions. A unidirectional fiber lamina can be considered transversely isotropic, and its elastic properties can be described with five independent constants [17]. The elastic properties of fiber composites are influenced by factors such as fiber orientation, material properties, volume fraction of fibers, thickness, and fiber distribution [3,4,18–21]. Fiber distribution can be broadly classified as random or regular, with the latter including square and hexagonal arrangements.

In practical applications, materials often need to resist loads in different directions. To meet multi-directional load requirements, unidirectional laminae are stacked together at different angles to form multi-directional laminates, allowing the material to resist multi-directional loads. Typical layups include cross-ply laminates, which consist of 0° and 90° plies, and angle-ply laminates, which include plies oriented at $\pm\theta$ (e.g., ±45°) [13]. The influence of these stacking sequences on the mechanical behaviour of laminates has been investigated intensively [22–26].To describe laminate stacking sequences, the terms symmetric and balanced are often used. A symmetric laminate has the same material, thickness, and orientation mirrored about the mid-plane, eliminating bending-extension coupling. A balanced laminate contains pairs of off-axis plies at $+\theta$ and $-\theta$, which helps minimize shear-extension coupling.

These tailored structural arrangements—combined with the intrinsic properties of fibers and matrices—have significant advantages, such as high stiffness-to-weight ratios, durability, resistance to corrosion, and design flexibility. These benefits have contributed to the adoption of fiber laminate composites across industries such as marine, civil engineering, aerospace, military, and automotive sectors [1–3,27].

In the construction sector, fiber-reinforced composites are increasingly used to improve the structural performance and durability of different elements. Mohamed et al. [28]

conducted both experimental and analytical investigations on reinforced concrete beams, demonstrating that the use of a bore-epoxy anchorage system significantly enhances shear strength. In the context of conservation engineering, AlMuhanna et al. [29] evaluated fiber-reinforced mortars for masonry buildings and found that fiber inclusion generally increased the ductility compared to conventional mixes.

Additionally, Khodadadi et al. [30] discussed the use of fiber reinforced polymers in concrete, focusing on their effectiveness in confinement, flexural strengthening, and crack control. Complementing these findings, Mohammed Yusuf et al. [31] highlighted the sustainability aspects of carbon fiber–reinforced polymers across building components—including slabs, beams, and columns—emphasizing their recyclability potential and environmental impact.

In military applications, fiber-reinforced composites are increasingly used to meet the demand for lightweight, high-performance protective systems. Alzahrani et al. [32] reviewed fiber-reinforced polymer composites used in body armor, helmets, and aircraft equipment, highlighting that the integration of hybrid composites—such as graphene fillers combined with banyan aerial root, jute and glass fibers—has improved the mechanical performance and energy absorption capabilities. Tsirogiannis et al. [33] demonstrated that composite armors enhanced with nanomaterials improve the mechanical strength and ballistic performance of military vehicles. In line with these studies, Bhat et al. [34] analyzed various armor systems—including fiber-reinforced polymer composites, metallic and multilayer configurations—and concluded that composite-based systems offer a reduction in weight and an increase in energy absorption. The design flexibility enables more effective load distribution, making composites a compelling alternative to traditional heavy metallic armor.

In the automotive field, composite materials are being explored for both structural performance and lightweight design [35–38]. Getu et al. [39] performed an impact analysis on a vehicle's internal door panel made from a bamboo–sisal fiber reinforced hybrid composite, demonstrating its potential for use in automotive interior applications. Extending this work, Zhang and Xu [40] provided a comprehensive review of lightweight automotive materials—ranging from high-strength steels to composites—highlighting composites as ideal candidates for both exterior and interior components.

2.2 Laminate Plate/Shell Theories

Plates, as a specific type of shell with zero curvature, can be analyzed using various shell theories. These theories simplify three-dimensional problems into two dimensions by defining how deformation occurs through thickness. This section discusses the Kirchhoff and Mindlin plate/shell theories, which are widely used equivalent single-layer approaches for modelling laminated structures. The relevant equations for these theories are presented later in the section 3.3.

2.2.1 Classical Laminated Plate Theory

Classical Laminated Plate Theory (CLT) is based on Kirchhoff's hypothesis. This theory assumes that the normal to the middle surface of the plate remains straight and perpendicular to the surface even after deformation [17] . As a result, transverse shear deformation is neglected, which makes the theory most appropriate for thin plates where shear effects are minimal.

2.2.2 First Order Shear Deformation Theory

The Mindlin Plate Theory, also known as the First-Order Shear Deformation Theory (FSDT), is an extension of classical plate theory (Kirchhoff theory) that accounts for the effects of transverse shear deformation [41]. Unlike Kirchhoff's theory, which assumes that normal to the mid-surface before deformation remains perpendicular to the mid-surface after deformation, the Mindlin theory relaxes this assumption. This makes it suitable for analyzing thicker plates where transverse shear effects become significant.

2.3 Micromechanics Models

This section introduces the micromechanics models that will be used later in this research. We discuss ten models in total: eight widely recognized models commonly applied in the study of unidirectional composites-Voigt-Reuss (VR), Hashin-Shtrikman (HS), Chamis, Halpin-Tsai (HT), Halpin-Tsai modified (HTm), Generalized Self-Consistent (GSC), Mori-Tanaka (MT) and Bridging Model (Br)-and two iterative models, iterative isotropized Voigt-Reuss bounds (Iter-Iso-VR) and iterative isotropized Hashin-Shtrikman bounds (Iter-Iso-HS), which have been recently developed and validated for particulate composites.

These models vary in their focus and application. Some are comprehensive, predicting all five key material properties of a transversely isotropic unidirectional lamina: the longitudinal Young's modulus (E_1), transverse Young's modulus (E_2), in-plane shear modulus (G_{12}), out-of-plane shear modulus (G_{23}), and in-plane Poisson's ratio (v_{12}). Others concentrate on improving the accuracy of one or two properties. Additionally, certain models incorporate empirical parameters, which need to be calibrated against experimental or FEM data to achieve more accurate predictions. The selected models are introduced below, with detailed equations provided later in the section 3.1.

2.3.1 Voigt-Reuss Models

The Voigt-Ruess model is a simple and widely used method in the literature. It consists of two models: the Voigt model [42], which assumes materials are in series, and the Reuss model [43], which assumes materials are in parallel. The Voigt model accurately predicts E_1 and v_{12}. However, the Reuss model does not accurately predict E_2, G_{12}, and G_{23}.

Many recent and more accurate models have been developed based on VR, where Chamis and HT are two popular modifications that will be discussed later [44]. These modifications usually used the same equations as Voigt-Ruess for E_1 and v_{12}; and tried to improve the prediction accuracy of one or more remaining properties. Therefore, the VR model is selected for this research as a reference point for comparison.

2.3.2 Hashin-Shtrikman Models

Hashin and Strikman [45] utilized variational principles along with polarization tensor to predict bounds for arbitrary phase geometry. This model introduced upper and lower bounds within which the properties of a material must lie.

In this research, we assess the accuracy of two recently developed iterative methods, which are based on iterations over the VR and HS bounds. The HS method is discussed here because it is a foundational basis for the iterative approach. However, this method is not used solely for predicting the five properties, as it provides bounds rather than exact solutions, also utilized in [4]

2.3.3 Chamis Model

Chamis [46] employs the same equations as the Voigt model to predict the longitudinal elastic modulus and in-plane Poisson ratio. For the other properties, Chamis introduces new formulas that incorporate the square root of the volume fraction. This method can predict all five properties and have greater accuracy compared with the Ruess model, making it a suitable choice for this research.

2.3.4 Halpin-Tsai Model

Halpin [47] discussed how environmental factors can influence the stiffness of materials. The model uses the same equations as VR for predicting E_1 and v_{12}. However, it does not provide an equation for predicting G_{23}. The model improves upon the VR predictions for E_2 and G_{12} by introducing empirical parameters. These parameters account for factors such as aspect ratio, reinforcement stiffness relative to matrix stiffness, volume fraction, inclusion geometries, and loading conditions. For a square distribution, Halpin proposed specific values for the parameter n: n=1 for G_{12} and n=2 for E_2; these values will be adopted in this study.

To achieve more accurate predictions, curve fitting may be necessary for different situations. For example, Hewitt and Malherbe [48] suggested an alternative reinforcement factor based on experimental data for an E-glass and polyester resin system, improving predictions at high volume fractions through curve fitting.

2.3.5 Halpin-Tsai modified Model

Giner et al. [49] proposed a new reinforcement factor, n=1.5, for volume fractions between 0.25 and 0.55, for randomly distributed unidirectional fibers, specifically for calculating E2 based on finite element analyses, provides a more realistic representation than the idealized square array distribution. The analysis procedure was verified by first comparing results against those for a square array configuration and through several sensitivity analyses.

This modification of the Halpin-Tsai model introduces a new reinforcement factor that is particularly relevant for this research, as it accounts for the random distribution of fibers, which is a consideration in the FEM simulations conducted here. This modification only applies to E_2, so the predictions for the other properties will remain consistent with the original HT model.

2.3.6 Generalized Self Consistent Model

Bounds and expressions for the effective elastic moduli of fiber-reinforced materials were initially derived using a variational method based on the classical principles of minimum potential energy and minimum complementary energy [50]. This work provided bounds for the out-of-plane shear modulus and exact expressions for four other properties. Building on this foundation, Hashin [51] extended the analysis by establishing bounds on three of the five independent effective elastic moduli, specifically the out-of-plane bulk modulus and the two shear moduli, with no geometric restrictions other than transverse isotropy.

Consistent with these bounding results, Christensen and Lo [52] proposed a solution for the transverse shear modulus. They utilized a three-phase model, which included the fiber, matrix, and an equivalent homogeneous medium. This model represented the fiber and matrix as two concentric cylinders embedded within an infinite medium with the combined properties of the fiber and matrix.

The Generalized Self Consistent predicts all five properties using the exact solution provided by Hashin and Rosen [50] and Christensen and Lo [52].

2.3.7 Mori-Tanaka Model

Mori and Tanaka [53] developed a method to find the average internal stress in the matrix of a material containing inclusions. Later, Benveniste [54] reformulated MT theory to compute the effective properties of composites, incorporating the equivalent inclusion concept introduced by Eshelby [55]. Building on this foundation, Abaimov et al. [56] provided a closed-form expression of the MT theory to predict the five engineering constants of unidirectional fiber-reinforced materials.

2.3.8 Bridging Model

In the Bridging model, the matrix is defined using Eshelby's inclusion method [8,9]. To determine the five elastic properties of unidirectional composites, E_1 and v_{12} are calculated using the same equations as VR, providing good accuracy without the need for empirical parameters. For the other properties, two empirical bridging parameters are introduced to account for fiber packing geometry, including factors such as the relative position of the fibers embedded in the resin, fiber volume fraction, and fiber cross-sectional shapes.

Wang and Huang [9] calculated averaged errors for 18 composites and recommended bridging parameters (α and β) of 0.3 as providing the most accurate overall results. This recommendation will be used in this research.

It is important to note that while there are recommendations for the values of these parameters, the prediction of elastic properties is sensitive to their selection. When the moduli of the fiber and matrix are comparable, this influence is minimal [9]. However, for composites with large differences between phase properties, the predictions can vary significantly depending on the choice of bridging parameters, as illustrated by Huang and Zhou [8].

2.3.9 Iter-Iso-VR and Iter-Iso-HS Models

The Isotropized Voigt-Reuss bounds (Iter-Iso-VR) and Iterative Isotropized Hashin-Shtrikman bounds (Iter-Iso-HS) models were developed by Luo [57] to remove the anisotropy between the VR and HS bounds and predict the effective elastic properties of isotropic materials. Originally applied to predict the mechanical properties of particulate composites, these models have been shown to be more accurate than other popular micromechanics models, particularly at high volume fractions of inclusions (around 80%) and when there are large contrasts between phase properties, as confirmed by both experimental data and finite element modelling.

In this research, these models are employed to predict E_2 and G_{23}, and their accuracy is evaluated for the first time in the context of fiber-reinforced composites.

2.4 Experimental Methods for Stiffness Characterization of Composite Materials

In this study, the finite element predictions are validated against a multi-method experimental investigation on glass–epoxy cross-ply laminates [58], which employed uniaxial tensile and three-point flexural testing, vibration, and Lamb-wave techniques. This section presents a literature review of both destructive and non-destructive approaches (including vibration-based and wave propagation methods), with emphasis on experimental techniques relevant to the validation of finite element results in the present work. The following sections discuss key findings from successful applications, along with common sources of error and limitations associated with each method.

2.4.1 Destructive Testing Methods

Destructive methods such as tensile, compression, shear, and bending tests, later used in the selected validation study, are widely used to characterize the mechanical properties of composite materials and remain the benchmark for obtaining laminate stiffness and serve as reference data for comparison with non-destructive methods. These tests are performed to generate load–deflection or load–elongation data, which are subsequently converted into the material's elastic properties. Standardized procedures for these tests, ASTM test methods[59–65], have been reviewed in [66–68].

Conducting these tests presents some challenges. For example, tensile testing of unidirectional composites is sensitive to fiber misalignment and improper gripping, which can introduce significant variability in the measured properties. In compression tests, the risk of buckling must be carefully managed, as it can compromise the accuracy of the results. A key limitation of existing shear test methods for composite materials is their inability to produce a pure and uniform shear stress distribution within the test section.

In the case of bending tests, a comparative study by El Messiry et al. [69] evaluated several methods for measuring the stiffness of unidirectional fibers. The study examined various techniques, such as three-point and four-point bending, cantilever-based testing, and the hanging pear loop method, across different fiber types, including polyester, carbon, Kevlar, Vectran, and glass. The results showed that the four-point bending test consistently yields higher and more reliable stiffness values, primarily due to its ability to reduce shear deformation and stress concentration. When it comes to testing laminate composites, additional complexities arise—one of the most prominent being the free-edge stress effect, which can influence the accuracy of results across various test methods [67].

Destructive tests, while reliable, are inherently invasive and cannot be applied without causing damage to the specimen. They are often more time-consuming, as multiple samples are required for a complete analysis. Moreover, they cannot be performed on installed or operating components, leading to additional material costs and preparation time for the samples. Therefore, several review studies have extensively discussed non-destructive methods as practical alternatives for evaluating composite stiffness [70–74].

2.4.2 Non-Destructive Methods Based on Wave Propagation

Wave propagation methods provide a non-destructive means of determining the elastic properties of composite materials and are generally classified into bulk-wave and guided-wave approaches [72]. Bulk waves are commonly used for thick composites, while guided waves—particularly Lamb waves which applied in the experimental study selected for laminate-level validation in this thesis —are more suitable for thin plates. At high frequencies, hundreds of kilohertz, the dispersive phase velocities of Lamb waves are measured along different directions of a composite plate and used in inverse analyses to extract elastic constants [58].

Wave Propagation technique has been employed to determine the elastic properties of composite materials. Zimmer and Cost [75] demonstrated early success in identifying five elastic moduli of a transversely isotropic unidirectional CFRP using ultrasonic testing. Castellano et al. [76] addressed some challenges in ultrasonic measurements—such as wave speed accuracy—using goniometric devices and ultrasonic immersion techniques to improve the characterization of unidirectional composites. In a separate study, Castellano et al. [77] applied ultrasonic immersion testing to multilayered anisotropic GFRP composites and showed that, despite the high sensitivity of moduli to wave speed errors, the results correlated well with those from standard destructive tests. Wu and Liu [78] introduced a hybrid approach where certain elastic constants were obtained via bulk wave ultrasonics, while the remaining were derived through inversion of Lamb wave dispersion.

Lamb wave–based methods have further expanded the capability to characterize complex laminates. Lasn et al. [79] retrieved eight out of nine engineering constants for a composite material using Lamb wave propagation. However, some limitations were noted: the shear modulus G_{12} could not be resolved, and the accuracy for certain constants (E_2, E_3 , and Poisson's ratios) was lower than for others. Jiang et al. [80] investigated the applicability of Lamb-wave-based techniques to cross-ply carbon fiber laminates and confirmed their accuracy through comparison with tensile tests and theoretical predictions. It was noted that the method is suitable for composites with in-plane Poisson's ratios below 0.3. In addition to the mentioned limitations, some drawbacks of the wave propagation methods are the dispersive nature of guided waves, the formation of multiple overlapping waveforms, and complex setup procedures [72].

2.4.3 Non-Destructive Methods Based on Vibration

Vibration-based methods, also utilized in the selected laminate experiment, assess the mechanical properties of laminates by analyzing their response to external excitations [58,72]. These methods involve low-frequency structural vibrations (generally up to a few thousand hertz) and enable the measurement of natural frequencies, modal damping, and the mode shapes. The stiffness properties can then be extracted using the natural frequencies.

Vibration-based methods have been shown to reliably determine the primary in-plane elastic properties of composite laminates, such as E_1, E_2, and G_{12}, with minimal discrepancies across various studies [81,82]. However, the accuracy diminishes for properties such as the transverse shear moduli G_{13} and G_{23}, particularly in thin plates where sensitivity to these moduli is low. Similarly, discrepancies in the Poisson's ratio ν_{12} have been reported, which aligns with low sensitivity of this parameter compared to the in-plane moduli [83]. These findings were also confirmed in studies involving unidirectional composites, where similar patterns of sensitivity and accuracy were observed [84].

Building on this, Gsell et al. [85] developed a fully automated procedure for determining five orthotropic stiffness components—two in-plane moduli and three shear moduli—using only out-of-plane vibrational data. In addition to material characterization, modal analysis using impulsive excitation techniques has demonstrated potential as a fast and efficient tool for quality control and structural assessment [86]. Despite effectiveness, the vibration method has some disadvantages, including complex procedures, reliance on bulky equipment, and a strong dependence on operator proficiency [80].

2.5 Finite Element Analysis in Composite Materials

The rapid progress in computational technology has enabled advancements in numerical analysis [87]. Given the inaccuracies in analytical methods [10,11], and the need to represent complex microstructures in greater detail [87], numerical methods have become increasingly important and are applied in many research studies. These advancements have made finite element modeling particularly valuable for predicting the elastic stiffness of composite materials. The following paragraphs review finite element analysis (FEA) studies relevant to the prediction of elastic stiffness in unidirectional and laminated composites.

Finite element modeling has been applied extensively to a wide range of fiber composites, including both natural and synthetic systems, to investigate their micromechanical behavior. In the case of natural fibers, FEM has been used to analyze tensile and flexural responses of flax fiber composites [88], bamboo [89], and luffa and palm [90], and to evaluate how structural parameters influence tensile performance [91]. Xiong et al. [92] discussed multiscale finite element modeling strategies for both natural fibers and their reinforced composites and how representative volume element (RVE) models at different length scales can capture fiber geometry.

Modeling approaches for synthetic fiber-reinforced composites with polymer matrices have also been widely explored. Matrix materials in composites can be polymers, metals, or ceramics, with polymer matrices being the most widely used due to their ease of processing, ability to form complex shapes, and relatively low tooling and manufacturing costs [93]. Finite element simulations have been employed to study their response under various loading conditions, including tensile and flexural. With many papers focused on mechanical properties of widely used carbon and glass fiber [94–102].

Kaushik et al. [103] conducted review on the numerical modeling of fiber-reinforced polymer composites, focusing on various loading conditions including tension, compression, flexural for high-performance fibers such as carbon, Kevlar, and glass, in both unidirectional and woven configurations. The review emphasized the FEM role as a cost-effective alternative to extensive experimental testing for design and analysis of textile composites, as pursued in the present work.

For laminated composite structures, Smolnicki et al. [104,105] reviewed recent FEM developments for layered systems, underscoring the importance of selecting the appropriate modeling scale (macro-, meso-, or microscopic) according to the objective of analysis. A more detailed laminate modeling strategy was presented by Song et al. [106], who proposed a multiscale simulation approach to predict the mechanical properties of orthogonally symmetric carbon fiber reinforced polymer laminates using the known properties of the fiber and matrix materials.

In their model [106], although the model operates at the macroscopic scale, it incorporates detailed microscale geometry by stacking unidirectional fiber-matrix models according to the ply orientations within the laminate. The authors used this method to calculate key engineering constants, including E_1, E_2, E_3, G_{12}, G_{31}, v_{12}, v_{23} and v_{31}, for cross-ply laminates. These results were then compared with predictions from analytical calculation (using Halpin–Tsai combined with Classical Laminate Theory) and available experimental data. The study reported good agreement for some properties, demonstrating the potential of the approach for accurate mechanical property prediction.

In addition to fiber orientation and material properties, the spatial distribution of fibers plays a key role in determining composite behavior. Different fiber distributions, random and regular (including square and hexagonal arrangements), have been analyzed in comparative studies by several researchers [4,19,107–113]. The analysis of composites with regular fiber distributions does not require intensive computing, but actual fiber distributions in manufactured composites often exhibit irregularity due to process-induced variability. Therefore, many studies have focused on generating random fiber distributions [114–124]

To analyze the behavior of composites, a Representative Volume Element (RVE) is widely used. Several studies have explored how to determine appropriate RVE sizes for different fiber configurations [125,126]. More recent works have incorporated uncertainty analysis into finite element modeling to assess how local variations in volume fraction and mesh density influence simulation results [127,128]. These studies highlight the importance of generating sufficiently large RVEs when modeling composites with randomly distributed fibers. In finite element modeling of composite materials, two common methods used to represent the microstructure are geometry-based finite element modeling (GB-FEM) and voxel-based finite element modeling (VB-FEM). In GB-FEM, the mesh follows the exact shape of each material region [129]. On the other hand, VB-FEM divides the model into uniform cubes (voxels) and assigns material properties based on each voxel's position relative to the underlying material phase.

While GB-FEM provides high geometric accuracy, it can introduce complications in generating a high-quality mesh [130]. Although adaptive meshing can improve geometry representation, it may significantly increase computational cost and still does not always guarantee mesh quality [131]. As a result, poor mesh quality can lead to increased numerical error in simulations. To overcome these limitations, VB-FEM uses a uniform grid structure that avoids element distortion and simplifies the meshing process.

Luo [129] and Doitrand [132] compared the two methods, showing convergence in the computed elastic properties. While GB-FEM has lower computational costs when inclusions are large and regularly distributed, VB-FEM is similarly efficient—and sometimes even more so—for small, randomly distributed inclusions. These advantages have led to its application across various material systems and disciplines. Sas et al. [133] developed a nonlinear voxel-based FE model to predict femoral strength in both healthy and metastatic bones. Their model showed high accuracy compared to experimental results and matched the performance of tetrahedral models, but with a faster, more automated workflow suitable for clinical use. VB-FEM has also been applied to study elastic behavior in various composite systems: Luo [129] investigated particulate composites, Gulfo et al. [134] and Ryatt and Ramulu [135,136] focused on complex morphologies, and Doitrand et al. and Schneider et al. [132,137] examined woven composites, all demonstrating the method's robustness and effectiveness for modeling complex mesostructures.

2.6 Summary of Literature Review and Identification of Research Objectives

The literature review discussed the composite materials, specifically laminated composites, and covered their structure, applications, and fundamental theories used to model their behaviour. Composite materials, composed of fibers and a matrix, exhibit enhanced stiffness and strength. Unidirectional and multi-directional fiber arrangements are discussed, highlighting their applications across industries, such as aerospace and automotive, and emphasizing the need for materials to withstand multi-directional loads.

For laminated structures, Classical Laminated Plate Theory (CLT) and First-Order Shear Deformation Theory (FSDT) are examined, where CLT applies to thin plates and FSDT to thicker plates. Additionally, various micromechanics models, including Voigt-Reuss, Chamis, Halpin-Tsai, and more advanced iterative models, are discussed for predicting mechanical properties. These models vary in prediction accuracy for parameters like elastic moduli and shear moduli, with certain models incorporating empirical parameters or iterative methods to refine results.

The review also emphasizes the significance of Finite Element Analysis (FEA) in composite behaviour prediction, particularly through Voxel-Based Finite Element Method (VB-FEM), which ensures mesh quality and is advantageous for materials with high inclusion densities.

The main objective of this thesis is to evaluate the accuracy and applicability of analytical micromechanics models in predicting the elastic properties of composite laminates. Building on the comparison of micromechanics models for unidirectional laminae, this research integrates the most accurate models with First-Order Shear Deformation Theory (FSDT) to predict the stiffness of symmetric cross-ply laminate plates. The performance of each analytical approach is assessed by comparing its predictions against a voxel-based finite element model, which serves as a numerical reference.

Chapter 3

Methodology

3.1 Micromechanics Models for Determine Effective Laminae Material Properties

In this section, the equations corresponding to each of the micromechanics models selected in Section 2.3 are presented. These include formulations for the five independent elastic constants of a transversely isotropic unidirectional lamina: the longitudinal modulus (E_1), transverse modulus (E_2), in-plane shear modulus (G_{12}), out-of-plane shear modulus (G_{23}), and in-plane Poisson's ratio (v_{12}), forming the mathematical foundation for the analyses conducted in this research. These models reviewed include Voigt-Reuss (VR), Hashin-Shtrikman (HS), Chamis, Halpin-Tsai (HT), Halpin-Tsai modified (HTm), Generalized Self-Consistent (GSC), Mori-Tanaka (MT), and the Bridging Model (Br). Additionally, two iterative models, the Iterative Isotropized Voigt-Reuss bounds (Iter-Iso-VR) and Iterative Isotropized Hashin-Shtrikman bounds (Iter-Iso-HS), are also included.

3.1.1 Voigt-Ruess Models

The Voigt model assumes that strain in the fiber direction in fiber, matrix, and composite are identical [93]. This assumption leads to the calculation of E_1 and ν_{12} for unidirectional composite materials, as expressed in equations(1) and (2) [44].

$$E_1 = E_1^f\, V_f + (1 - V_f)E^m \tag{1}$$

$$\nu_{12} = \nu_{12}^f\, V_f + (1 - V_f)\nu^m \tag{2}$$

On the other hand, the Reuss model assumes that stress in fiber, matrix, and composite are identical [93]. This model is used to predict E_2, G_{12}, and G_{23}, as in equations (*3*) - (*5*) [44].

$$E_2 = \frac{E_2^f\, E^m}{E_2^f(1 - V_f) + E^m V_f} \tag{3}$$

$$G_{12} = \frac{G_{12}^f\, G^m}{G_{12}^f(1 - V_f) + G^m V_f} \tag{4}$$

$$G_{23} = \frac{G_{23}^f\, G^m}{G_{23}^f(1 - V_f) + G^m V_f} \tag{5}$$

3.1.2 Hashin-Strikman Models

Hashin-Strikman predicts bounds predict bounds for arbitrary phase geometry as equation (6)-(9)[45]. Elastic modulus bounds can then be predicted using elasticity relations in equation (10) [57].

$$G_L = G_m + \frac{V_f}{\left[\frac{1}{G_f - G_m} + \frac{6(1 - V_f)(K_m + 2G_m)}{5G_m(3K_m + 4G_m)}\right]} \tag{6}$$

$$G_U = G_f + \frac{(1 - V_f)}{\left[\frac{1}{G_m - G_f} + \frac{6V_f(K_f + 2G_f)}{5G_f(3K_f + 4G_f)}\right]} \tag{7}$$

$$K_L = K_m + \frac{V_f}{\left[\frac{1}{K_f - K_m} + \frac{(1 - V_f)}{K_m + \frac{4}{3}G_m)}\right]} \tag{8}$$

$$K_U = K_f + \frac{(1 - V_f)}{\left[\frac{1}{K_m - K_f} + \frac{V_f}{K_f + \frac{4}{3}G_f)}\right]} \tag{9}$$

$$E = \frac{9KG}{3K + G} \tag{10}$$

3.1.3 Chamis Model

Chamis used same equations as the VR model to predict longitudinal elastic modulus and in-plane Poisson's ratio and for other properties, the equations are given as (11)-(13) [46].

$$E_2 = \frac{E^m}{1 - \sqrt{V_f}\,[1 - (E^m/E_2^f)]} \tag{11}$$

$$G_{12} = \frac{G^m}{1 - \sqrt{V_f}\,[1 - (G^m/G_{12}^f)]} \tag{12}$$

$$G_{23} = \frac{G^m}{1 - \sqrt{V_f}\,[1 - (G^m/G_{23}^f)]} \tag{13}$$

3.1.4 Halpin-Tsai Model

Halpin-Tsai use same equations as the VR model to predict longitudinal elastic modulus and in-plane Poisson's ratio and for transversal elastic modulus and in-plane shear modulus uses two empirical parameters ζ_{E_2} and ζ_{G_2} to account for environmental factors, equations and parameters and initially suggested parameters are indicated in (14)-(19) [47]. This method initially consider square array distribution of fibers.

$$E_2 = E^m \left(\frac{1 + \zeta_{E_2} \eta_{E_2} V_f}{1 - \eta_{E_2} V_f} \right) \tag{14}$$

$$G_{12} = G^m \left(\frac{1 + \zeta_{G_{12}} \eta_{G_{12}} V_f}{1 - \eta_{G_{12}} V_f} \right) \tag{15}$$

$$\eta_{E_2} = \frac{(E_2^f / E^m) - 1}{(E_2^f / E^m) + \zeta_{E_2}} \tag{16}$$

$$\eta_{G_{12}} = \frac{(G_{12}^f / G^m) - 1}{(G_{12}^f / G^m) + \zeta_{G_{12}}} \tag{17}$$

$$\zeta_{E_2} = 2 \tag{18}$$

$$\zeta_{G_{12}} = 1 \tag{19}$$

3.1.5 Halpin-Tsai modified Model

Halpin-Tsai modified proposed new parameter for transversal elastic modulus considering a random distribution of fibers the new parameter is shown as equation (*20*) [49].

$$\zeta_{E_2} = \begin{cases} 4.924 - 35.888V_f + 125.118V_f^2 - 145.121V_f^3 & \text{if } V_f < 0.3 \\ 1.5 + 5500V_f^{18} & \text{if } V_f \geq 0.3 \end{cases} \tag{20}$$

3.1.6 Generalized Self-Consistent Model

Generalized self consistent method build on the assumption of three phase material, Equations shown as (21)-(43) [138,139]:

$$E_1 = E_1^f\, V_f + E^m(1 - V_f) + \frac{4V_f(1 - V_f)\left(\nu_{12}^f - \nu^m\right)^2}{\frac{(1 - V_f)}{K_{23}^f} + \frac{V_f}{K^m} + \frac{1}{G^m}} \tag{21}$$

$$\nu_{12} = \nu_{12}^f\, V_f + \nu^m(1 - V_f) + \frac{V_f(1 - V_f)\left(\nu_{12}^f - \nu^m\right)^2\left(\frac{1}{K^m} - \frac{1}{K_{23}^f}\right)}{\frac{(1 - V_f)}{K_{23}^f} + \frac{V_f}{K^m} + \frac{1}{G^m}} \tag{22}$$

$$K_{23} = K^m + \frac{V_f}{\frac{1}{K_{23}^f - K^m} + \frac{1 - V_f}{K^m + G^m}} \tag{23}$$

$$G_{12} = G^m\, \frac{G_{12}^f(1 + V_f) + G^m(1 - V_f)}{G_{12}^f(1 - V_f) + G^m(1 + V_f)} \tag{24}$$

$$G_{23} = G^m \left(\frac{-B + \sqrt{B^2 - 4AC}}{2A} \right) \tag{25}$$

$$A = a_0 + a_1 V_f + a_2 V_f^2 + a_3 V_f^3 + a_4 V_f^4 \tag{26}$$

$$B = b_0 + b_1 V_f + b_2 V_f^2 + b_3 V_f^3 + b_4 V_f^4 \tag{27}$$

$$C = c_0 + c_1 V_f + c_2 V_f^2 + c_3 V_f^3 + c_4 V_f^4 \tag{28}$$

$$a_0 = -2(G^m)^2(2G^m + K^m)[2G_{23}^f G^m + K_{23}^f(G_{23}^f + G^m)][2G_{23}^f G^m + K^m(G_{23}^f + G^m)] \tag{29}$$

$$a_1 = 8(G^m)^2(G_{23}^f - G^m)[2G_{23}^f G^m + K_{23}^f(G_{23}^f + G^m)][(G^m)^2 + G^m K^m + (K^m)^2] \tag{30}$$

$$a_2 = -12(G^m)^2(K^m)^2(G_{23}^f - G^m)[2G_{23}^f G^m + K_{23}^f(G_{23}^f + G^m)] \tag{31}$$

$$a_3 = 8(G^m)^2\{(G_{23}^f G^m)^2 K_{23}^f + (G_{23}^f)^2 G^m K^m (K_{23}^f - G^m) + (K^m)^2 [G_{23}^f G^m (G_{23}^f - 2G^m) + K_{23}^f (G_{23}^f - G^m)(G_{23}^f + G^m)]\} \tag{32}$$

$$a_4 = 2(G^m)^2(G_{23}^f - G^m)(2G^m + K^m)[K_{23}^f G^m K^m - G_{23}^f(2G^m(K_{23}^f - K^m) + K_{23}^f K^m)] \tag{33}$$

$$b_0 = 4(G^m)^3 \left[2G_{23}^f G^m + K_{23}^f\left(G_{23}^f + G^m\right)\right] \left[2G_{23}^f G^m + K^m\left(G_{23}^f + G^m\right)\right] \tag{34}$$

$$b_1 = 8(G^m)^2 K^m \left(G_{23}^f - G^m\right) \left[2G_{23}^f G^m + \left(G_{23}^f + G^m\right) K_{23}^f\right](G^m - K^m) \tag{35}$$

$$b_2 = -2a_2 \tag{36}$$

$$b_3 = -2a_3 \tag{37}$$

$$b_4 = -4(G^m)^3\left(G_{23}^f - G^m\right)\left\{K_{23}^f G^m K^m - G_{23}^f\left[2G^m\left(K_{23}^f - K^m\right) + K_{23}^f K^m\right]\right\} \tag{38}$$

$$c_0 = 2(G^m)^2 K^m\left[2G_{23}^f G^m + K_{23}^f\left(G_{23}^f + G^m\right)\right]\left[2G_{23}^f G^m + K^m\left(G_{23}^f + G^m\right)\right] \tag{39}$$

$$c_1 = 8(G^m K^m)^2\left(G_{23}^f - G^m\right)\left[2G_{23}^f G^m + K_{23}^f\left(G_{23}^f + G^m\right)\right] \tag{40}$$

$$c_2 = a_2 \tag{41}$$

$$c_3 = a_3 \tag{42}$$

$$c_4 = -2(G^m)^2 K^m\left(G_{23}^f - G^m\right)\left\{K_{23}^f G^m K^m - G_{23}^f\left[2G^m\left(K_{23}^f - K^m\right) + K_{23}^f K^m\right]\right\} \tag{43}$$

3.1.7 Mori-Tanaka Model

Based on average internal stress and equivalent inclusion idea, Mori-Tanaka predicts fove properties using equations (44)-(52) [11,56].

$$E_1 = V_f E_1^f + (1 - V_f)\, E^m + 2V_f(1 - V_f)\, Z_1\left(\nu_{12}^f - \nu^m\right)^2 \tag{44}$$

$$E_2 = \frac{E_1}{[1 - (\nu^m)^2]\,(Y_1 + Y_2)} \tag{45}$$

$$\nu_{12} = \nu^m + 2V_f \frac{Z_1}{E^m}\left(\nu_{12}^f - \nu^m\right)[1 - (\nu^m)^2] \tag{46}$$

$$G_{12} = \frac{G^m}{2(1 - V_f)(1 + \nu^m)}\left[1 + V_f - \frac{4V_f}{1 + V_f + 2(1 - V_f)\frac{G_{12}^f}{E^m}(1 + \nu^m)}\right] \tag{47}$$

$$G_{23} = E^m\left\{2(1 + \nu^m) + \frac{V_f}{\frac{1 - V_f}{8[1 - (\nu^m)^2]} + \frac{G_{23}^f}{E^m - 2G_{23}^f(1 + \nu^m)}}\right\}^{-1} \tag{48}$$

$$Y_1 = V_f Z_1\left(\frac{E_1^f}{E^m}\right)\left[\frac{1 + \nu^m}{E^m} - \frac{2}{E_1^f} + \frac{1 + \nu_{23}^f}{E_2^f}\right] \tag{49}$$

$$Y_2 = \frac{1}{1 - (\nu^m)^2} + 2V_f\left(\frac{E_1}{Z_2}\right)\left[1 + \nu_{23}^f - \frac{E_2^f}{E^m}(1 - \nu^m)\right] \tag{50}$$

$$Z_1 = \left\{-2(1 - V_f)\frac{\left(\nu_{23}^f\right)^2}{E_1^f} + (1 - V_f)\frac{1 - \nu_{23}^f}{E_2^f} + \frac{(1 + \nu^m)[1 + V_f(1 - 2\nu^m)]}{E^m}\right\}^{-1} \tag{51}$$

$$Z_2 = E_2^f(3 + V_f - 4\nu^m)(1 + \nu^m) + (1 - V_f)E^m(1 + \nu_{23}^f) \tag{52}$$

3.1.8 Bridging Model

The bridging model predicts all five properties as in equations (53)-(61) (Huang & Zhou, 2011; Vignoli et al., 2019). E_1 and v_{12} match those of the VR model, while the other properties depend on two empirical bridging parameters to account for fiber packing geometry. For these empirical parameters, we used the recommendations of Wang and Huang indicated in equation (62) [9].

$$E_1 = V_f E_1^f + (1 - V_f)\, E^m \tag{53}$$

$$\nu_{12} = V_f \nu_{12}^f + (1 - V_f)\, \nu^m \tag{54}$$

$$E_2 = \frac{[V_f + (1 - V_f)\, a_{11}][V_f + (1 - V_f)\, a_{22}]}{[V_f + (1 - V_f)\, a_{11}]\left[\left(\frac{V_f}{E_2^f}\right) + \left(\frac{1 - V_f}{E^m}\right) a_{22}\right] + V_f(1 - V_f)\left[\left(\frac{\nu_{12}^f}{E_1^f}\right) + \left(\frac{\nu^m}{E^m}\right)\right] a_{12}} \tag{55}$$

$$G_{12} = \frac{V_f + (1 - V_f)\, a_{66}}{\left(\frac{V_f}{G_{12}^f}\right) + \left(\frac{1 - V_f}{G^m}\right) a_{66}} \tag{56}$$

$$G_{23} = \frac{V_f + (1 - V_f)\, a_{22}}{\left(\frac{V_f}{G_{23}^f}\right) + \left(\frac{1 - V_f}{G^m}\right) a_{22}} \tag{57}$$

$$a_{11} = E^m / E_1^f \tag{58}$$

$$a_{22} = \beta + (1-\beta)\left(E^m/E_2^f\right) \tag{59}$$

$$a_{66} = \alpha + (1-\alpha)\left(G^m/G_{12}^f\right) \tag{60}$$

$$a_{12} = \left(\frac{E_1^f \nu^m - E^m \nu_{12}^f}{E^f{}_1 - E^m}\right)(a_{11} - a_{22}) \tag{61}$$

$$\alpha = \beta = 0.3 \tag{62}$$

3.1.9 Iter-Iso-VR and Iter-Iso-HS Models

The Iter-Iso-VR and Iter-Iso-HS models removed anisotropy between the VR and HS bounds. These models are used in this research to predict E_2 and G_{23} for fiber-reinforced composites [57].

Equations (*63*) and (*64*)implement Iter-Iso-VR using the conditions of $E_U^{(i)} > E_L^{(i)}$ and $(f_1 + f_2) = 1$.[57]

$$E_U^{(i+1)} = f_1 E_L^{(i)} + f_2 E_U^{(i)} \tag{63}$$

$$E_L^{(i+1)} = \frac{E_L^{(i)} E_U^{(i)}}{f_2 E_L^{(i)} + f_1 E_U^{(i)}} \tag{64}$$

Equation (*65*)-(*72*) implement Iter-Iso-HS, using the conditions of $K_U^{(i)} > K_L^{(i)}$, $G_U^{(i)} > G_L^{(i)}$ and $0 < (f_1, f_2) < 1$.

$$K_L^{(i+1)} = K_L^{(i)} + \alpha_L^{(i)} \tag{65}$$

$$\alpha_L^{(i)} = \frac{f_2\left(K_U^{(i)} - K_L^{(i)}\right)\left(3K_L^{(i)} + 4G_L^{(i)}\right)}{3f_2K_L^{(i)} + 3f_1K_U^{(i)} + 4G_L^{(i)}} \tag{66}$$

$$K_U^{(i+1)} = K_U^{(i)} + \alpha_U^{(i)} \tag{67}$$

$$\alpha_U^{(i)} = \frac{f_1\left(K_U^{(i)} - K_L^{(i)}\right)\left(3K_U^{(i)} + 4G_U^{(i)}\right)}{3f_1K_U^{(i)} + 3f_2K_L^{(i)} + 4G_U^{(i)}} \tag{68}$$

$$G_L^{(i+1)} = G_L^{(i)} + \beta_L^{(i)} \tag{69}$$

$$\beta_L^{(i)} = \frac{5f_2\left(G_U^{(i)} - G_L^{(i)}\right)G_L^{(i)}\left(3K_L^{(i)} + 4G_L^{(i)}\right)}{(12f_2+8)\left(G_L^{(i)}\right)^2 + \left(12f_1G_U^{(i)} + (6f_2+9)K_L^{(i)}\right)G_L^{(i)} + 6G_U^{(i)}K_L^{(i)}f_1} \tag{70}$$

$$G_U^{(i+1)} = G_U^{(i)} - \beta_U^{(i)} \tag{71}$$

$$\beta_U^{(i)} = \frac{5f_1\left(G_U^{(i)} - G_L^{(i)}\right)G_U^{(i)}\left(3K_U^{(i)} + 4G_U^{(i)}\right)}{(12f_1+8)\left(G_U^{(i)}\right)^2 + \left(12f_2G_L^{(i)} + (6f_1+9)K_U^{(i)}\right)G_U^{(i)} + 6G_L^{(i)}K_U^{(i)}f_2} \tag{72}$$

3.2 Characterization of Unidirectional Composite Using Voxel-Based Finite Element Modeling

This section outlines the numerical characterization of unidirectional composites using voxel-based finite element modeling (VB-FEM) to determine the five key elastic constants—E_1, E_2, G_{12}, G_{23}, v_{12}—by RVE with randomly distributed fibers. The workflow involves generating fiber coordinates using a custom MATLAB algorithm, meshing and assigning materials in ANSYS APDL, and applying specific boundary conditions to extract effective mechanical properties.

3.2.1 Geometry Creation

A MATLAB (R2023a) code was developed to generate randomly distributed fibers. The rand() function was used to generate the coordinates of fiber centers, which are placed sequentially within a loop and stored in an array until reaching a desired volume fraction Figure 1 shows an RVE with randomly distributed fibers, with Figure 1a showing of the coordinate system.

Using the developed MATLAB code, a volume fraction of about 60% can be achieved with fibers of identical diameters. Gusev et al. [140] investigated the effect of fiber diameter variation on elastic properties by comparing fibers with identical and variable diameters, maintaining a fixed volume fraction of 54%. Their comparison showed that the effect of fiber diameter variations on the composite elastic constants is very small. Melro et al.

[4] studied the impact of RVE length to fiber radius on elastic properties of unidirectional composites, reporting that by increasing the ratio, the longitudinal properties remain unaffected while the transverse properties converge. Based on these findings, fibers with variable diameters are used in this study to achieve fiber volume fractions greater than 60% after conducting a convergence study for the transverse properties in section 4.1.1.

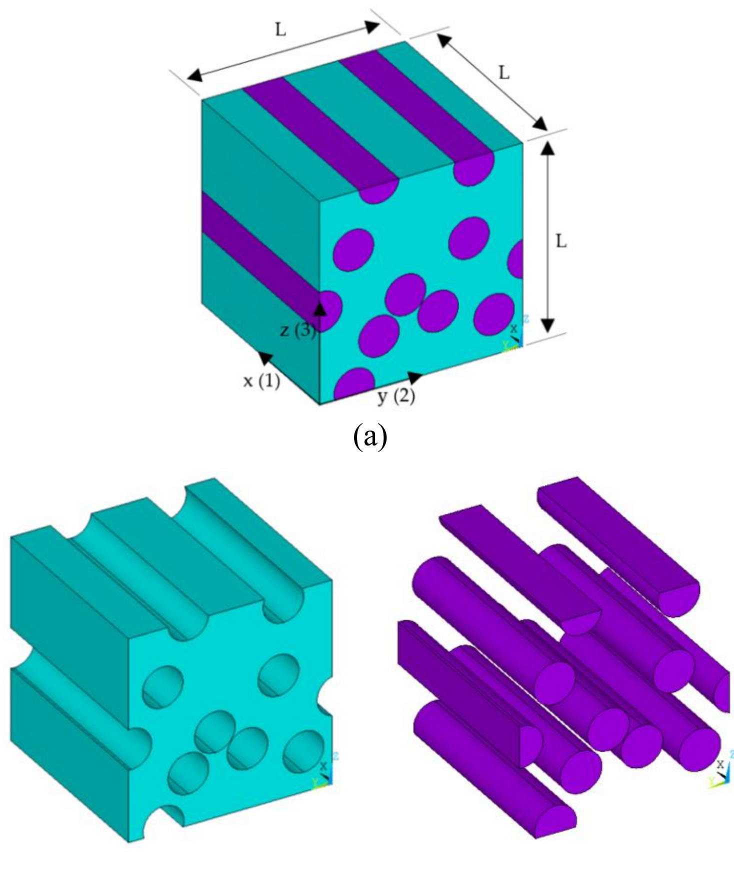

(a)

(b) (c)

Figure 1. Random fiber distribution in a representative volume element (RVE): (a) complete RVE, (b) matrix phase, and (c) fiber phase

To accomplish this, fiber generation begins with the maximum target radius within the RVE. A variable named 'number of attempts' is introduced, which specifies the number of unsuccessful placement attempts allowed before reducing the fiber radius. As the available space within the RVE decreases, the number of attempts required to successfully place a fiber naturally increases. This process continues across all radii between the predetermined maximum and minimum values until either the desired volume fraction is reached or no additional fibers can be placed after the set number of attempts. Figure 2 shows two examples of the generated RVEs with different fiber radius profiles.

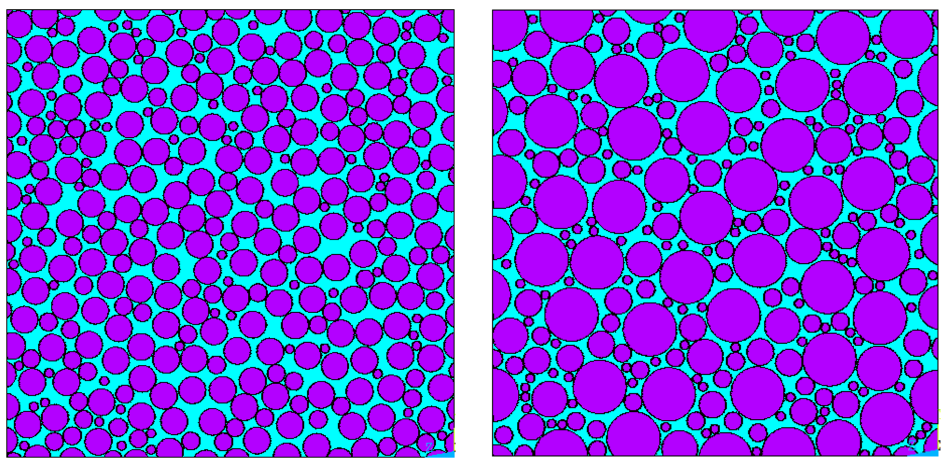

(a) (b)

Figure 2. Randomly distributed fibers with different radii with volume fractions of a) 65%, and b) 73%

3.2.2 Meshing and Material Assignment

The meshing and material assignment process involves creating a voxel-based finite element model that reflects the microstructure of the composite RVE. Here, VB-FEM modeling is performed using ANSYS APDL (2022 R2, ANSYS, Inc., Canonsburg, USA), based on the fiber coordinates and radii generated in MATLAB (R2023a). The fiber composite material is modeled as glass–epoxy and carbon–epoxy, using the material properties described in section 3.5. The process starts by creating a uniform cubic mesh (voxels), using eight-node brick elements. Initially, the matrix property is assigned to all elements. In the next step, based on the known coordinates and radii of fibers, each voxel is either reassigned the fiber property or remains as matrix material, depending on its location in the RVE. A 2D view of the 3D meshed RVE before and after fiber material assignment is shown in Figure 3. Moreover, a 3D visualization of the full RVE, along with separate views highlighting only the fiber phase and only the matrix phase, is presented in Figure *4*.

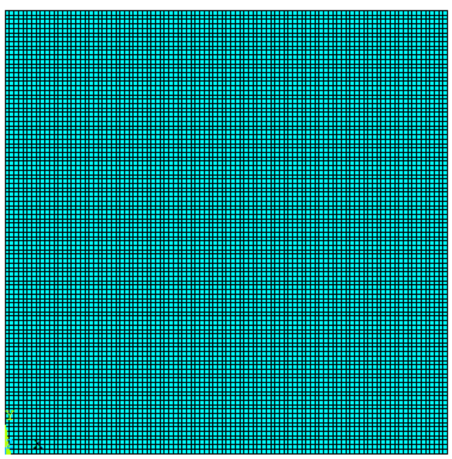

(a)

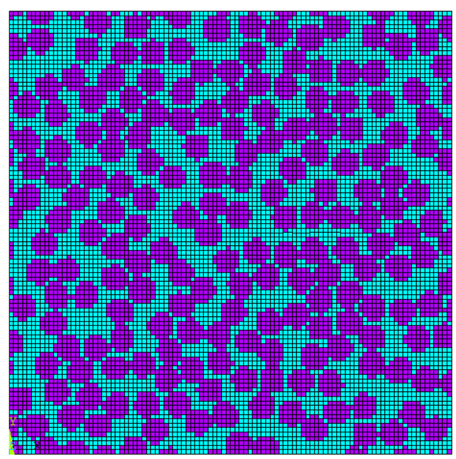

(b)

Figure 3. Meshed RVE: (**a**) before material assignment, (b) after assigning fiber and matrix material properties.

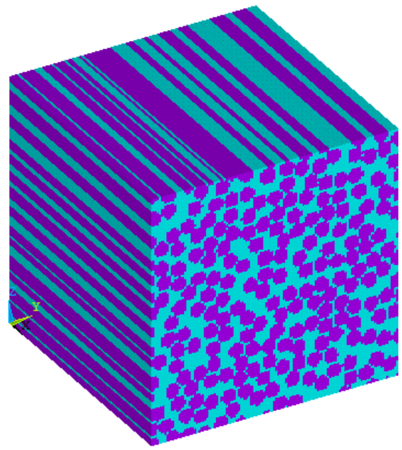

(a)

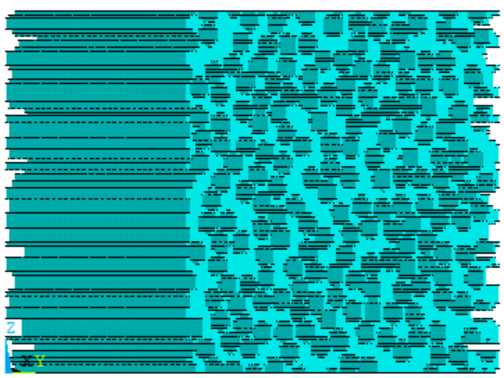

(b)

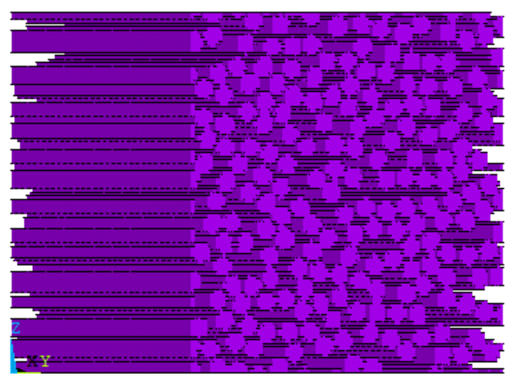

(c)

Figure 4. Three-dimensional voxel-based meshed RVE showing (**a**) full volume, (**b**) matrix phase, and (**c**) fiber phase.

3.2.3 Boundary Conditions and Post-Processing

Boundary conditions are applied following the work in [141] and summarized in Table *1*, to predict Young's modulus (E_i), Poisson's ratio (υ_{ij}), and shear modulus (G_{ij}), along the three axial directions ($i,\ j\ =\ x,\ y,\ z$), where the origin of the coordinate system is placed at one vertex of the RVE, with the three coordinate axes along the adjacent edges. The length of the RVE is set to 100 units. For surfaces where coupled degrees of freedom (DOFs) are specified, the displacement in the corresponding direction is constrained to be identical.

Table 1. Boundary Conditions [57]

RVE Surface	**Young's Modulus (E_i) and Poisson's Ratio (υ_{ij})**			**Shear Modulus (G_{ij})**		
	$E_x, \upsilon_{xy}, \upsilon_{xz}$	**$E_y, \upsilon_{yx}, \upsilon_{yz}$**	**$E_z, \upsilon_{zx}, \upsilon_{zy}$**	**G_{xy}**	**G_{yz}**	**G_{zx}**
x = 0	$u_x = 0$	$u_x = 0$	$u_x = 0$	$u_x = u_y = u_z = 0$	Free	Free
y = 0	$u_y = 0$	$u_y = 0$	$u_y = 0$	Free	$u_x = u_y = u_z = 0$	Free
z = 0	$u_z = 0$	$u_z = 0$	$u_z = 0$	Free	Free	$u_x = u_y = u_z = 0$
x = 100	$u_x = 1$	u_x(coupled DOFs)	u_x(coupled DOFs)	$u_y = 1$, u_x(coupled DOFs)	Free	Free
y = 100	u_y (coupled DOFs)	$u_y = 1$	u_y (coupled DOFs)	Free	$u_z = 1$, u_y (coupled DOFs)	Free
z = 100	u_x (coupled DOFs)	u_x (coupled DOFs)	$u_z = 1$	Free	Free	$u_x = 1$, u_z (coupled DOFs)

In this study, periodic boundary conditions are not applied because uniform displacement constraints are enforced across opposing faces of the RVE. While the RVE geometry may not appear periodic (e.g., with non-complementary inclusions at boundaries), the displacement coupling ensures an average uniform strain field, which is sufficient to extract effective elastic properties under first-order homogenization principles. This approach is consistent with that of Luo [142], where periodicity was not imposed geometrically but was shown to be unnecessary under displacement-driven boundary conditions commonly adopted in numerical homogenization frameworks.

After solving the finite element equations for nodal displacements, the elastic properties of the RVE such as Young's modulus, Poisson's ratio, and shear modulus are calculated using Equations (*73*)-(*76*).

$$E_i = \frac{\overline{\sigma_i}}{\overline{\varepsilon_i}}, \qquad (i = x, y, z) \tag{73}$$

$$\upsilon_{ij} = -\frac{\overline{\varepsilon_j}}{\overline{\varepsilon_i}}, \qquad (i, j = x, y, z) \tag{74}$$

$$G_{ij} = -\frac{\overline{\tau_{ij}}}{\overline{\gamma_{ij}}}, \qquad (i, j = x, y, z) \tag{75}$$

$$\overline{\sigma_i} = \int_V \sigma_i \, dV, \qquad \overline{\varepsilon_i} = \int_V \varepsilon_i \, dV, \qquad \overline{\tau_{ij}} = \int_V \tau_{ij} \, dV, \qquad \overline{\gamma_{ij}} = \int_V \gamma_{ij} \, dV \tag{76}$$

Here, σ_i, ε_i, τ_{ij}, γ_{ij}, and V are normal stress, normal strain, shear stress, shear strain and volume of the RVE, respectively

3.3 Laminate Plate/Shell Stiffness Equations

The stiffness parameters of a laminate plate or shell are determined by first evaluating the mechanical properties of each lamina, or layer, which is typically a unidirectional composite. For each layer, the effective material properties—such as the longitudinal and transverse Young's moduli (E_1 and E_2), Poisson's ratios (ν_{12}), and shear moduli (G_{12} and G_{23})—are defined based on the fiber and matrix constituents using micromechanics models.

Next, these properties are used to form two stiffness matrices. Since composite laminates are made up of multiple layers oriented at different angles, the stiffness matrix for each layer is transformed to a global coordinate system. This transformation accounts for the fiber orientation in each layer, using a transformation matrix that rotates the stiffness properties from the lamina's local coordinates to the laminate's global coordinates.

Once the stiffness matrices for all the layers are transformed, the overall laminate stiffness is calculated by integrating the contributions from each layer across the thickness of the laminate. This process results in the formation of four stiffness matrices: the in-plane stiffness matrix (A), the bending stiffness matrix (D), the coupling matrix (B) and the transverse shear stiffness matrix (H).

Finally, the mechanical properties of the laminate, such as its effective Young's moduli, shear moduli, and Poisson's ratios in different directions, were determined from these matrices. The detailed steps taken, along with the equations, are given in this section [17,143,144].

For a transversely isotropic material Hook's law gives the compliance matrix as in equation (*77*).

$$\begin{bmatrix}\epsilon_1\\ \epsilon_2\\ \epsilon_3\\ \gamma_4\\ \gamma_5\\ \gamma_6\end{bmatrix}=\begin{bmatrix}S_{11} & S_{12} & S_{12} & 0 & 0 & 0\\ S_{12} & S_{22} & S_{23} & 0 & 0 & 0\\ S_{12} & S_{23} & S_{22} & 0 & 0 & 0\\ 0 & 0 & 0 & (S_{22}-S_{23})/2 & 0 & 0\\ 0 & 0 & 0 & 0 & S_{66} & 0\\ 0 & 0 & 0 & 0 & 0 & S_{66}\end{bmatrix}\begin{bmatrix}\sigma_1\\ \sigma_2\\ \sigma_3\\ \sigma_4\\ \sigma_5\\ \sigma_6\end{bmatrix} \tag{77}$$

Writing the compliance matrix as the five independent engineering constants that describe unidirectional composites we have equation (*78*).

$$S=\begin{bmatrix}\frac{1}{E_1} & -\frac{\upsilon_{12}}{E_1} & -\frac{\upsilon_{12}}{E_1} & 0 & 0 & 0\\ -\frac{\upsilon_{12}}{E_1} & \frac{1}{E_2} & \frac{1}{E_2}-\frac{1}{2G_{23}} & 0 & 0 & 0\\ -\frac{\upsilon_{12}}{E_1} & \frac{1}{E_2}-\frac{1}{2G_{23}} & \frac{1}{E_2} & 0 & 0 & 0\\ 0 & 0 & 0 & \frac{1}{G_{23}} & 0 & 0\\ 0 & 0 & 0 & 0 & \frac{1}{G_{12}} & 0\\ 0 & 0 & 0 & 0 & 0 & \frac{1}{G_{12}}\end{bmatrix} \tag{78}$$

Both FSDT and CLT state that the change in thickness of the plate/shell can be neglected. Setting $\sigma_3 = 0$. Therefore, the compliance matrix reduces from 3D to plane stress in the equation (79).

$$S = \begin{bmatrix} \frac{1}{E_1} & -\frac{\upsilon_{12}}{E_1} & 0 & 0 & 0 \\ -\frac{\upsilon_{12}}{E_1} & \frac{1}{E_2} & 0 & 0 & 0 \\ 0 & 0 & \frac{1}{G_{23}} & 0 & 0 \\ 0 & 0 & 0 & \frac{1}{G_{12}} & 0 \\ 0 & 0 & 0 & 0 & \frac{1}{G_{12}} \end{bmatrix} \tag{79}$$

CLT additionally ignore the transverse shear, setting $\sigma_4 = \sigma_5 = 0$. Therefore, for CLT the compliance matrix will be reduced to a three-by-three matrix as (80).

$$S = \begin{bmatrix} \frac{1}{E_1} & -\frac{\upsilon_{12}}{E_1} & 0 \\ -\frac{\upsilon_{12}}{E_1} & \frac{1}{E_2} & 0 \\ 0 & 0 & \frac{1}{G_{12}} \end{bmatrix} \tag{80}$$

For FSDT the two remaining equations give (81) compliance matrix.

$$S^* = \begin{bmatrix} \frac{1}{G_{23}} & 0 \\ 0 & \frac{1}{G_{12}} \end{bmatrix} \tag{81}$$

The stiffness matrix C and C^* are then computed inverting the compliance matrix.

$$C = [S]^{-1} \tag{82}$$

After finding stiffness matrix C and C^* for a lamina, the coordinate system transfers from the lamina coordinate system to the laminate coordinate using the transformation matrix as given in (83) for C and in (84) for C^*:

$$T(\theta) = \begin{bmatrix} \cos\theta^2 & \sin\theta^2 & 2\cos\theta\sin\theta \\ \sin\theta^2 & \cos\theta^2 & -2\cos\theta\sin\theta \\ -\cos\theta\sin\theta & \cos\theta\sin\theta & \cos\theta^2 - \sin\theta^2 \end{bmatrix} \tag{83}$$

$$T^* = \begin{bmatrix} \cos\theta & \sin\theta \\ -\sin\theta & \cos\theta \end{bmatrix} \tag{84}$$

Transformed stiffness matrix $\bar{Q}$ and $\bar{Q}^*$ would be calculated as (85).

$$\bar{Q} = [T]^{-1}[Q][T]^{-T} \tag{85}$$

Then, A, B, D, H matrixes can be derived from following equations (86)-(89).

$$A_{ij} = \sum_{k=1}^{N} \left(\bar{Q}_{ij}\right)_k t_k; \qquad i,j = 1,2,6 \tag{86}$$

$$B_{ij} = \sum_{k=1}^{N} \left(\bar{Q}_{ij}\right)_k t_k \bar{z}_k; \qquad i,j = 1,2,6 \tag{87}$$

$$D_{ij} = \sum_{k=1}^{N} \left(\bar{Q}_{ij}\right)_k \left(t_k \bar{z}_k^2 + \frac{t_k^3}{12}\right); \qquad i,j = 1,2,6 \tag{88}$$

$$H_{ij} = \frac{5}{4}\sum_{k=1}^{N} \left(\bar{Q}_{ij}^*\right)_k [t_k - \frac{4}{t^2}(t_k \bar{z}_k^2 + \frac{t_k^3}{12}); \qquad i,j = 4,5 \tag{89}$$

Here, N is the total number of laminas in the laminate. $\left(\bar{Q}_{ij}\right)_k$ is $[\bar{Q}]$ matrix of kth lamina. is the distance from the midplane to the top of the jth lamina and h_j is the distance from the midplain to the bottom of the jth lamina. t_k is the thickness of lamina k, and $\bar{z}_k$ is the coordinate of the middle surface of the kth lamina.

Matrix A is called in-plane stiffness matrix connecting in-plane strains to in-plane forces in the laminate, using this matrix and considering a balanced symmetric laminate where $A_{13} = A_{23} = 0$, we can extract the in-plane properties of the laminate as in the equations (90)-(93):

$$E_x = \frac{A_{11}A_{22} - A_{12}^2}{h\,A_{22}} \tag{90}$$

$$E_y = \frac{A_{11}A_{22} - A_{12}^2}{h\,A_{11}} \tag{91}$$

$$\nu_{xy} = \frac{A_{12}}{A_{22}} \tag{92}$$

$$G_{xy} = \frac{A_{33}}{t} \tag{93}$$

For a balanced symmetric laminate the bending-extension coupling matrix, B, which relates in-plane strains to bending moments and curvatures to in-plane forces, is equal to zero. To extract equivalent bending modulus, the bending stiffness matrix, D, can be used to establish the relationship between curvatures and bending moments. Using the bending stiffness matrix of the laminate we can compute equivalent elastic properies as in equations (94)-(97).

$$.\,E_x^f = \frac{12(D_{11}D_{22} - D_{12}^2)}{t^3 D_{22}} \tag{94}$$

$$E_y^f = \frac{12(D_{11}D_{22} - D_{12}^2)}{t^3 D_{11}} \tag{95}$$

$$\nu_{xy}^{f} = \frac{D_{12}}{D_{22}} \tag{96}$$

$$G_{xy}^{f} = 12\frac{D_{33}}{t^3} \tag{97}$$

To find the transverse shear stiffness of the laminate H matrix can be utilized, which is called the transverse shear stiffness matrix linking transverse shear strains to transverse shear forces. The shear moduli can be extracted from H matrix using equations (98) and (99).

$$G_{yz} = \frac{H_{11}}{t} \tag{98}$$

$$G_{xz} = \frac{H_{22}}{t} \tag{99}$$

3.4 Characterization of Laminate Plate/Shell Stiffness Parameters Using Voxel-Based Finite Element Modeling

Building upon the methodology established for unidirectional composites, this section extends the voxel-based finite element modeling framework to the analysis of laminated composites. The goal is to evaluate laminate-level stiffness parameters—including in-plane, bending, and transverse shear matrices—by modeling the full three-dimensional microstructure of a symmetric cross-ply laminate. A six-layer [90/90/0/0/90/90] stacking sequence is considered, with distinct fiber distributions in each layer to reflect realistic manufacturing variability. the modeling workflow involves generating the geometry for the laminate, assigning appropriate material properties, and applying boundary conditions designed to extract the full set of laminate stiffness parameters.

3.4.1 Geometry Creation

A six-layer symmetric laminate with a [90/90/0/0/90/90] stacking sequence is modeled. The laminate consists of three distinct unidirectional fiber layers, each having a different random distribution of fibers to capture the natural variability in fiber placement. Although the fiber distributions differ, the fiber volume fraction for each layer is closely controlled to remain nearly identical, with variations kept within approximately 1%. To maintain laminate symmetry, the remaining three layers are created by mirroring the initial three layers.

The fiber centers were generated using the same MATLAB code described in section 3.2. For the laminate, an additional constraint was introduced: fibers were restricted to remain within the top and bottom boundaries of each layer, corresponding to the layer thickness, but were allowed to pass through the left and right boundaries, reflecting the material continuity along the length and width directions of the laminate.

The overall laminate was assembled by stacking the generated layers together, forming a composite structure with dimensions of $100 \times 100 \times 600$ units. This approach to constructing a laminate by stacking distinct layers was previously adopted by Song et al. [106]. The resulting RVE and its coordinate system is shown in Figure 5, with Figure 6 picture the fibers and matrix separately.

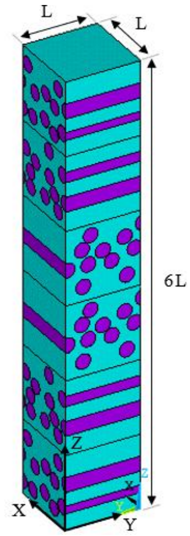

Figure 5. RVE and coordinate system for 6-layer laminate with fiber radius of 10 units, 30% fiber volume fraction, and a [90/90/0/0/90/90] layup

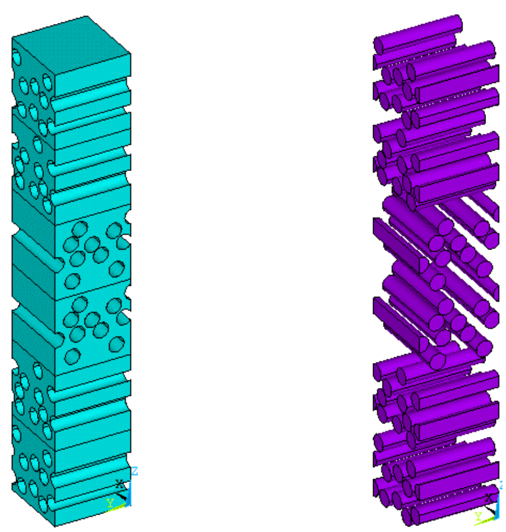

(a) (b)

Figure 6. 6-layer laminate with fiber radius of 10 units, 30% fiber volume fraction, and a [90/90/0/0/90/90] layup configuration: (a) matrix only, (b) fibers only.

3.4.2 Meshing and Material Assignment

The fiber coordinates and radii generated in MATLAB (R2023a) are used to construct the finite element model in ANSYS APDL (2022 R2, ANSYS, Inc., Canonsburg, USA). The laminate phase properties are indicated in section 3.5.2. Each layer is meshed uniformly one by one. During meshing, a local coordinate system is assigned to each layer based on its fiber orientation relative to the global coordinate system, ensuring that the correct material properties are later assigned. Elements located within the fiber regions are identified based on the fiber center positions and assigned the fiber material. Figure 7 shows the meshed RVE, with the matrix and fiber phases displayed separately in Figure 8.

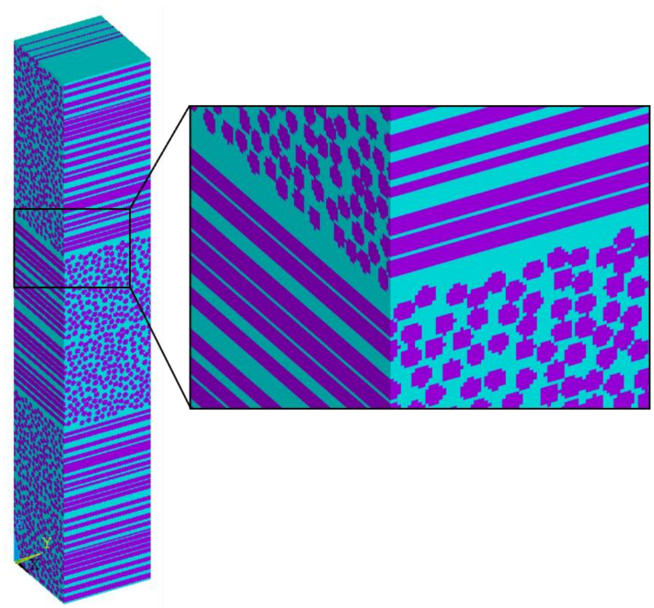

Figure 7. 6-layer meshed laminate with a fiber radius of 3 units, 50% fiber volume fraction, a [90/90/0/0/90/90] layup, and a resolution of 100 × 100 × 600 voxels

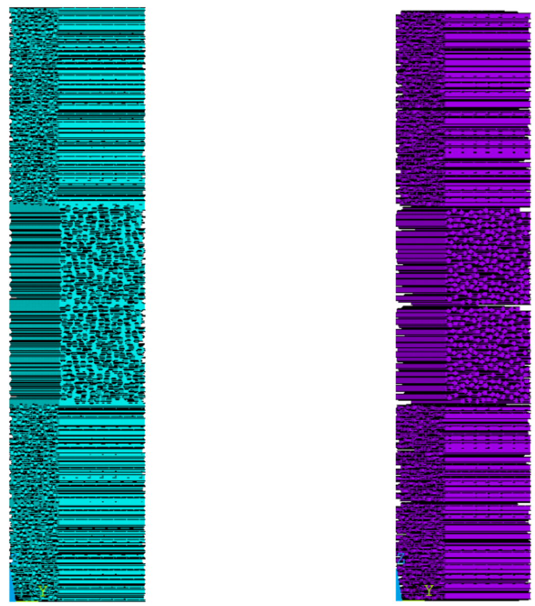

(a) (b)

Figure 8. (a) Matrix and (b) Fiber in a voxel-based model of a 6-layer laminate, with a fiber radius of 3 units, 50% fiber volume fraction, a [90/90/0/0/90/90] layup, and a resolution of 100 × 100 × 600 voxels

3.4.3 Boundary Conditions and Post-Processing for Predicting In-Plane Stiffness Matrix Parameters

To extract the in-plane stiffness matrix components of the laminate, three separate loading cases are applied to the RVE, each corresponding to a distinct in-plane deformation: uniaxial tension in the x-direction, uniaxial tension in the y-direction, and pure shear in the xy-plane. For each case, appropriate displacement boundary conditions are applied as shown in Table *2*.

Table 2. Boundary conditions applied for extracting in-plane stiffness parameters

RVE Surface	In-Plane Modulus		
	E_x, υ_{xy}	E_y	G_{xy}
x = 300	$u_x = 0$	$u_x = 0$	$u_x = u_y = 0$
y = 300	$u_y = 0$	$u_y = 0$	$u_y = \frac{x}{L}$
z = 300	$u_z = 0$	$u_z = 0$	$u_z = 0$
x = 0	$u_x = 1$	u_x (coupled DOFs)	$u_y = 1$, u_x (coupled DOFs)
y = 0	u_y(coupled DOFs)	$u_y = 1$	$u_y = \frac{x}{L}$
z = 0	Free	Free	Free

After simulation, the four in-plane properties (E_x, E_y, G_{xy}, ν_{xy}) are calculated from equations (73)-(76). These values are then substituted into equations (100)-(103) to compute the corresponding laminate in-plane stiffness matrix elements.

$$A_{11} = \frac{tE_x^2}{E_x - \nu_{xy}^2 E_y} \tag{100}$$

$$A_{22} = \frac{t\,E_x E_y}{E_x - \nu_{xy}^2 E_y} \tag{101}$$

$$A_{12} = \nu_{xy} A_{22} \tag{102}$$

$$A_{33} = t\,G_{xy} \tag{103}$$

3.4.4 Boundary Conditions and Post-Processing for Predicting Bending Stiffness Matrix Parameters

To evaluate the bending stiffness components of the laminate, simulations are performed using displacement control that induces bending (by applying linear curvature in the laminate) and twisting deformations. Table *3* summarizes the boundary conditions used to extract flexural moduli and flexural Poisson's ratio, and Figure 9 illustrates the implementation of a displacement constraint (used in Table *3*) applied to keep the surface flat both before and after deformation.

Table 3. Boundary conditions applied for extracting bending stiffness parameters

RVE	**Bending Modulus**		
Surface	E_x^f, υ_{xy}^f	E_y^f	G_{xy}^f
x = 300	$u_x = 0$	$u_x = 0$	$u_x = u_y = u_z = 0$
y = 300	$u_y = 0$	$u_y = 0$	Free
z = 300	$u_z = 0$	$u_z = 0$	Free
x = 0	$u_x = -\frac{z}{3L}$	Figure 9	$u_x = 0, u_y = -\frac{z}{6L} + 0.5, u_z = \frac{y}{6L} - 0.5$
y = 0	Figure 9	$u_y = -\frac{z}{3L}$	Free
z = 0	Free	Free	Free

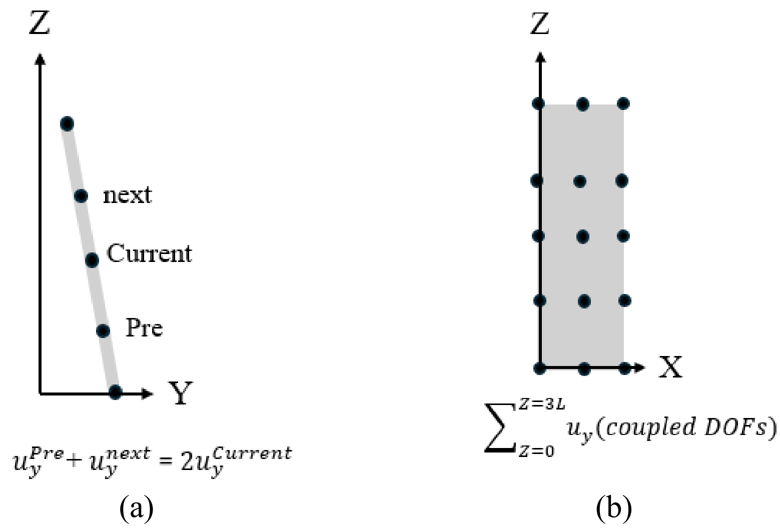

Figure 9. Displacement boundary conditions applied to preserve the planarity of a surface before and after deformation. The two views, (a) and (b), illustrate the same boundary setup from different perspectives.

Following the simulation, average stresses are extracted using ANSYS post-processing tools, and the flexural properties are calculated using equations (73)-(76). These values are then substituted into the following relations (Equations (104)-(107)) to obtain the bending stiffness matrix components:

$$D_{11} = \frac{t^3 {E_x^f}^2}{E_x^f - {\upsilon_{xy}^f}^2 E_y^f} \tag{104}$$

$$D_{22} = \frac{t^3 E_x^f E_y^f}{E_x^f - {\upsilon_{xy}^f}^2 E_y^f} \tag{105}$$

$$D_{12} = \upsilon_{xy}^f D_{22} \tag{106}$$

$$D_{33} = t^3 G_{xy}^f \tag{107}$$

3.4.5 Boundary Conditions and Post-Processing for Predicting transverse shear stiffness matrix Parameters

Displacement boundary conditions are applied to, as detailed in Table 4 to find effective shear moduli of the laminate.

Table 4. Boundary conditions applied for extracting transverse shear stiffness parameters

RVE Surface	Shear Modulus G_{yz}	Shear Modulus G_{xz}
x = 300	u_x (coupled DOFs)	$u_y = \frac{z}{3L}$
y = 300	$u_y = \frac{z}{3L}$	u_y (coupled DOFs)
z = 300	$u_x = u_y = u_z = 0$	$u_x = u_y = u_z = 0$
x = 0	u_x (coupled DOFs)	$u_y = \frac{z}{3L}$
y = 0	$u_y = \frac{z}{3L}$	u_y (coupled DOFs)
z = 0	$u_y = 1$, u_z (coupled DOFs)	$u_x = 1$, u_z (coupled DOFs)

Once the simulations are completed, the effective shear moduli are computed using equations (73)-(76). The final laminate-level transverse shear stiffness values are calculated as (equations (*108*) and (*109*)):

$$H_{11} = t\,G_{yz} \tag{108}$$

$$H_{22} = t\,G_{xz} \tag{109}$$

3.5 Experimental Cases for Validation

This section presents the experimental cases selected to validate the stiffness predictions obtained from micromechanics models and the voxel-based finite element model (VB-FEM) developed in this study. Validation is carried out at both the unidirectional and laminate levels. For unidirectional composites, two material systems—carbon–epoxy and glass–epoxy—are considered to assess model performance across a range of fiber–matrix property contrasts. For laminate-level analysis, a symmetric glass–epoxy cross-ply configuration is selected based on available experimental data. Details of each case, including material properties, layups, and data sources, are provided in the following subsections.

3.5.1 Experimental Cases Selected for Validation of Unidirectional Composites

For unidirectional composite validation, two material systems—carbon–epoxy and glass–epoxy—were selected to examine the effect of fiber–matrix property contrast on model predictions. These cases represent low and high contrasts in transverse stiffness, respectively, allowing assessment of micromechanics models and the voxel-based finite element model (VB-FEM) under different material conditions. The glass–epoxy elastic properties are shown in Table 5.

Table 5. Phase Properties of Glass-Epoxy [145]

Materials	Young's Modulus (GPa)	Shear Modulus (GPa)	Poisson Ratio
Glass Fiber	73.1	29.95	0.22
Epoxy II	3.45	1.28	0.35

In the carbon–epoxy case, the carbon fibers are modeled as transversely isotropic, with E_1 representing the Young's modulus along the fiber direction and E_2 representing the modulus transverse to the fiber direction, as listed in Table 6.

Table 6. Phase Properties of Carbon-Epoxy [145]

Materials	Young's Modulus (GPa)		Shear Modulus (GPa)	Poisson Ratio	
	E_1	E_2	G_{12}	υ_{12}	υ_{23}
Carbon Fiber	232	15	24	0.279	0.49
Epoxy I	5.35		1.97	0.354	

3.5.2 Experimental Case Selected for Validation of Laminate Plate/Shell

To validate the laminate-level predictions from the voxel-based finite element model (VB-FEM), an experimental study on a glass–epoxy symmetric cross-ply laminate was selected. In the chosen study, three independent experimental techniques— Uniaxial tensile and three-point flexural testing testing, natural frequency measurements, and Lamb wave dispersion analysis—were used to characterize the stiffness of glass fiber laminates. This multi-method approach provided a robust set of measured properties for comparison.

The [90/90/0/0/90/90] stacking sequence used in the experimental study was adopted for the laminate configuration modeled in this work The average values obtained from the three experimental techniques are depicted in Table 7.

Table 7. Elastic properties of Glass-Epoxy laminate with volume fraction of 0.58 [58]

Layup	E_x(GPa)	E_y(GPa)	E_x^f(GPa)	E_y^f(GPa)
[90/90/0/0/90/90]	21.97	33.03	13.97	38.83

The epoxy material used in the laminate was Epikote MGS RIMR 135 cured with Epikure MGS RIMH 137. Since the original paper did not report the matrix properties, values were extracted from a separate study; the properties used are listed in Table 8. For the E-glass fibers, the same properties reported in the unidirectional experimental case (Section 3.5.1) were used also listed in Table 8.

Table 8. Phase properties of Glass–epoxy used for laminate validation. Epoxy properties were taken from [146], and glass fiber properties from [145]

Materials	Young's Modulus (GPa)	Shear Modulus (GPa)	Poisson Ratio
Glass Fiber	73.1	29.95	0.22
Epoxy III	3.24	1.19	0.36

Chapter 4

Results and Discussion

4.1 Results Related to Unidirectional Laminae

In this section we first investigate the influence of fiber length-to-diameter (aspect) ratio on the transverse properties of unidirectional composites to establish a suitable geometric configuration for subsequent simulations. We then present a comprehensive comparison of various micromechanical models (as detailed in Section 3.1) with voxel-based finite element simulations (Section 3.2) and for two experimental cases (section 3.5.1). These comparisons aim to highlight the strengths and limitations of the micromechanical models in predicting the five elastic properties of unidirectional composites -(longitudinal Young's modulus (E_1), transverse Young's modulus (E_2), in-plane shear modulus (G_{12}), out-of-plane shear modulus (G_{23}), and in-plane Poisson's ratio (v_{12})-, providing a clear understanding of how these models align with or diverge from FEM simulations and experimental data.

4.1.1 Effect of Fiber Length-to-Diameter Ratio on Transverse Properties

To study the effect of fiber aspect ratio on transverse properties, different fiber diameters were used while keeping the fiber volume fraction constant at 40%. To reduce the influence of microstructural variability, four distinct RVEs were generated and simulated for each fiber diameter. The effective transverse elastic properties were then obtained by averaging the results across these four configurations. Figure 10 illustrates examples of fiber distributions corresponding to aspect ratios of 2.78, 8.33, and 16.67. Each RVE, including those shown in Figure 10, contained several non-overlapping fibers and was used in finite element simulations.

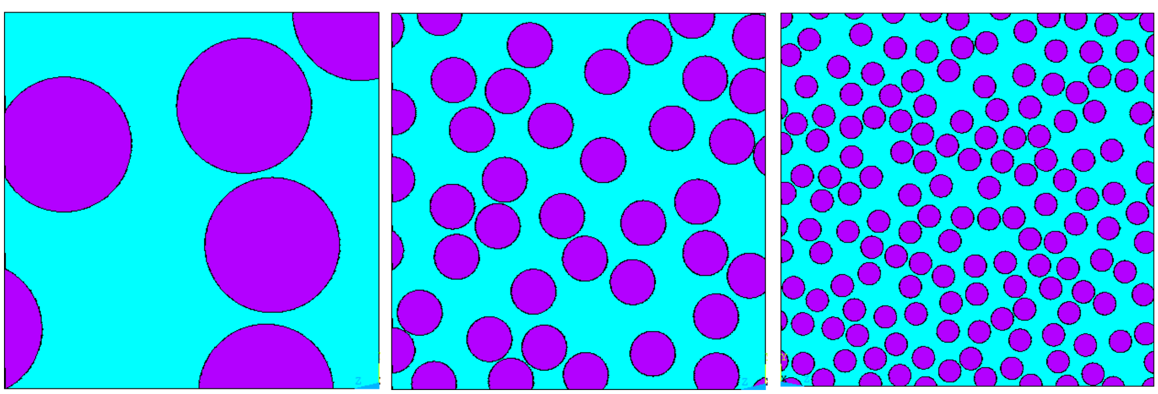

(a) (b) (c)

Figure 10. Examples of randomly generated fiber distributions at 40% volume fraction with fiber aspect ratios of (a) 2.78, (b) 8.33, and (c) 16.67. Each configuration shown was used in finite element simulations to compute effective properties. For each aspect ratio, four different RVEs were simulated and their results averaged to ensure statistical robustness.

Figure 11 and Figure 12 shows the effect of fiber aspect ratio on the transverse Young's modulus and transverse shear modulus of a glass–epoxy composite at a fixed fiber volume fraction of 40%, demonstrating that effect of increasing the fiber aspect ratio on the variability of the predicted properties and on their average values. The figures illustrate that as the fiber aspect ratio exceeds 8.33, the variance in the results continues decreasing, while the mean modulus values remain relatively stable. This stabilization effect is more pronounced for the transverse shear modulus than for the transverse Young's modulus. To minimize result variability, fibers with an aspect ratio of 16.67, corresponding to a fiber radius of 3 units in an RVE of 100 units, are used in the main simulations. For cases requiring volume fractions greater than 60%, fibers with a maximum radius of six units, corresponding to an aspect ratio of 8.33, are used in this study.

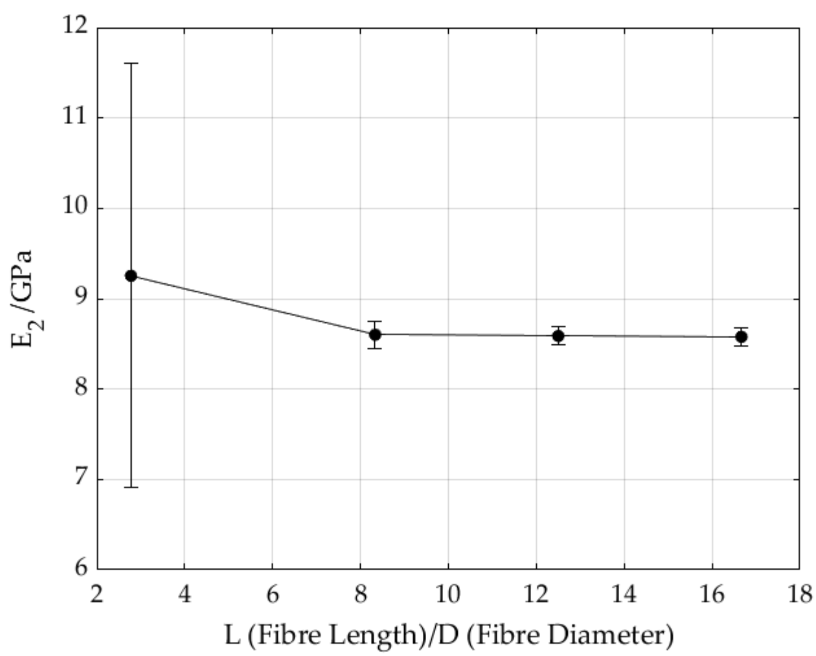

Figure 11. Effect of fiber aspect ratio on the transverse E_2 of a glass–epoxy composite at 40% fiber volume fraction.

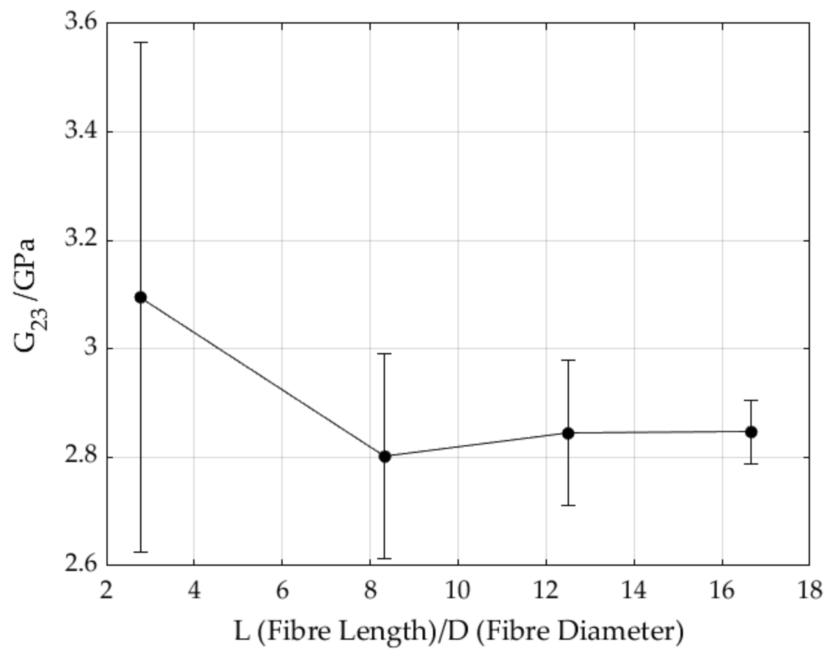

Figure 12. Effect of fiber aspect ratio on G_{23} of a glass–epoxy composite at 40% fiber volume fraction.

4.1.2 Carbon Epoxy

This subsection presents the results for the carbon–epoxy composite, focusing on the five independent elastic properties. Due to the relatively low contrast between carbon fiber and epoxy matrix properties in the transverse direction, this case is useful for evaluating the sensitivity and accuracy of different predictive models. Comparisons are made between micromechanics predictions, VB-FEM results, and experimental data across a range of fiber volume fractions.

1. Young's moduli E_1 and E_2

As illustrated in Figure 13, predicting the longitudinal Young's modulus (E_1), as expected, all the micromechanics models have the same accuracy, aligning closely with both numerical results and experimental data.

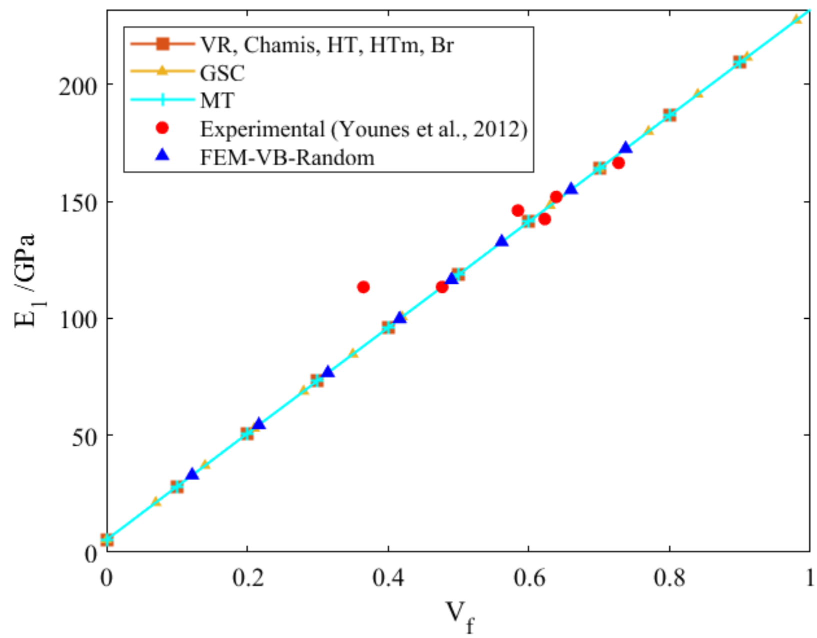

Figure 13. Comparison of micromechanics model, VB-FEM results, and experimental data for E_1 of a carbon–epoxy composite [145].

Moving to the transverse Young's modulus (E2) (Figure *14*), the numerical results are in good agreement with the experimental data. Among the nine micromechanics models plotted, Voigt-Ruess showed the least accuracy. For volume fractions less than 50%, the Mori-Tanaka (MT) and Generalized Self-Consistent Model (GSCM) were closest to the FEM data, the Bridging (Br) and Chamis models predicted higher values, while other models predicted lower values. As the volume fraction increased beyond 50%, the Iterative Isotropic Hashin-Shtrikman (Iter-Iso-HS) model aligned more closely with FEM data, except for the Halpin-Tsai modified (HTm) model, which deviated from the trend, while the other models predicted values that were in closer agreement.

Comparing the iterative models, the predictions from Iter-Iso-HS align more closely with FEM results than those from Iter-Iso-VR. For fiber volume fractions above 50%, the accuracy of both Iter-Iso-VR and Iter-Iso-HS models increases, particularly for Iter-Iso-HS, where its accuracy surpasses that of other models.

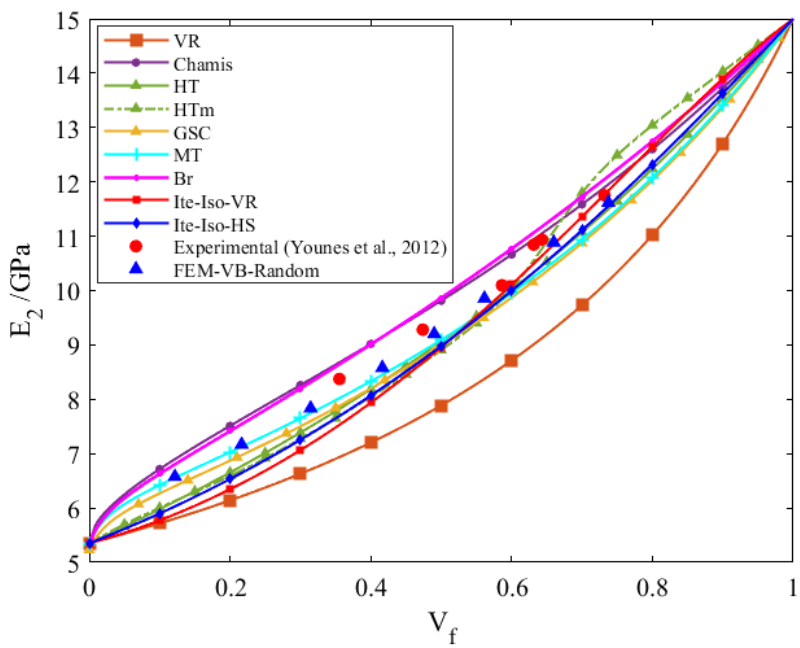

Figure 14. Comparison of micromechanics model, VB-FEM results, and experimental data for E_2 of a carbon–epoxy composite [145].

2. Shear moduli G_{12} and G_{23}

Investigate the longitudinal shear modulus (G_{12}) (Figure 15), numerical and experimental results match for low volume fractions of fibers, predicting results close to all micromechanics models except Voigt-Reuss, but increasing the fiber volume fraction results from numerical simulation get higher than the experimental data. Considering the experimental data, Mori-Tanaka, Halpin-Tsai and GSCM are the most accurate model. While using FEM as reference bridging model would be chosen.

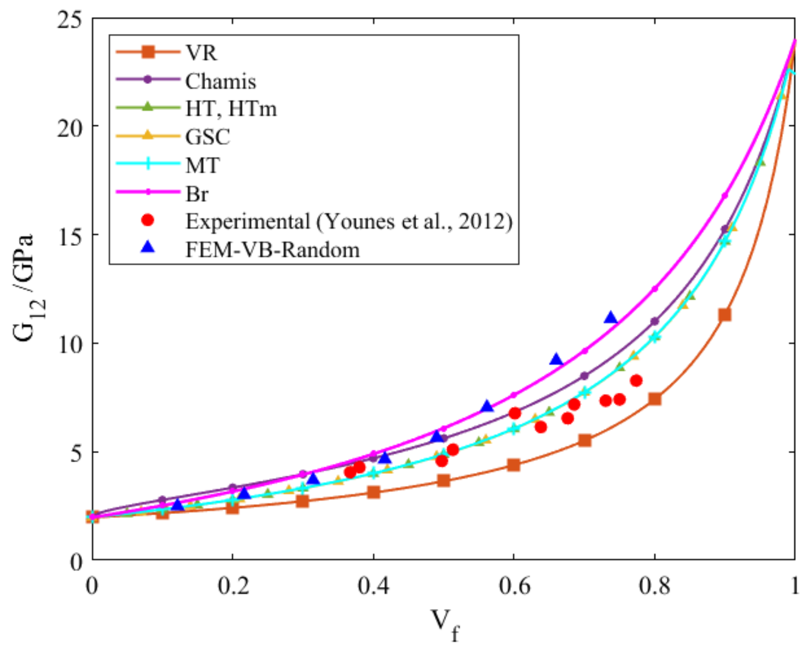

Figure 15. Comparison of micromechanics model, VB-FEM results, and experimental data for G_{12} of a carbon–epoxy composite [145].

For the out-of-plane shear modulus (Figure 16), most micromechanical models, except for the Voigt-Ruess and Chamis models, show good agreement with the experimental and FEM results. A closer examination of the experimental data reveals that iterative models are in closer alignment. Notably, the bridging model converges with the Iter-Iso-HS model at high-volume fractions. When considering only the FEM results, the MT and GSCM models exhibit the closest alignment.

1. Poisson’s ratio v_{12}

For the in-plane Poisson's ratio (Figure 17), all models provide accurate predictions. Among them, the MT and GSCM models match most closely with the FEM data.

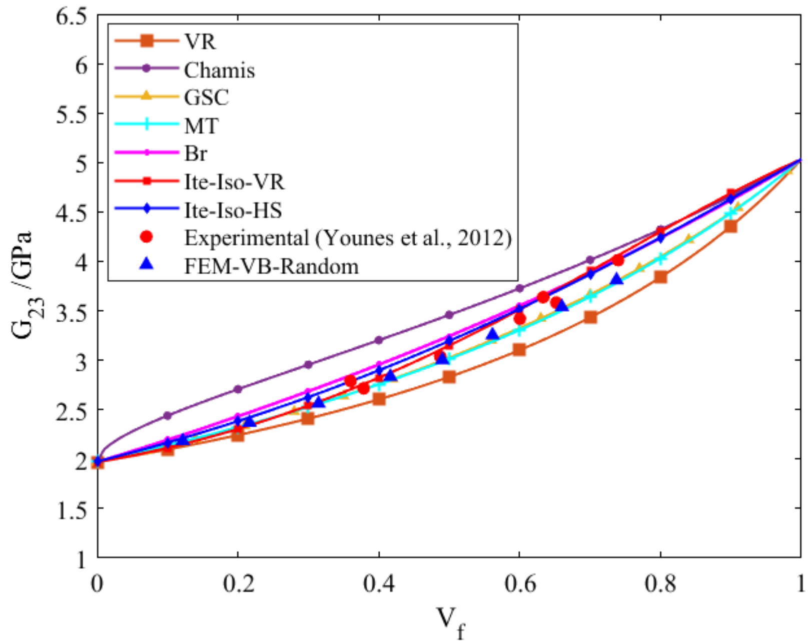

Figure 16. Comparison of micromechanics model, VB-FEM results, and experimental data for G_{23} of a carbon–epoxy composite [145].

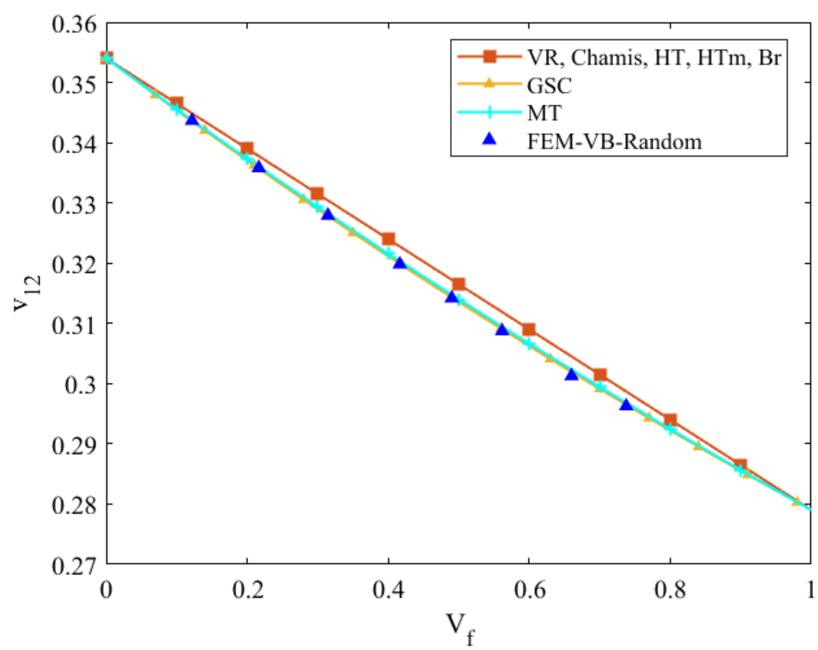

Figure 17. Comparison of micromechanics model and VB-FEM results for v_{12} of a carbon–epoxy composite.

4.1.3 Glass Epoxy

This subsection examines the performance of micromechanics models and VB-FEM in predicting the elastic properties of a glass–epoxy composite. Because of the higher contrast between the stiffness of glass fibers and the epoxy matrix, this case is expected to amplify differences among the models, particularly in the transverse and shear directions. The results are compared with available experimental data to assess the accuracy and limitations of each predictive approach.

1. Young's moduli E1 and E2

For the Glass Epoxy material, the longitudinal Young's modulus (E1) (Figure 18) is consistently predicted with accuracy by all micromechanics models, each aligning closely with the FEM results, demonstrating reliable performance similar to that observed with the Carbon Epoxy material.

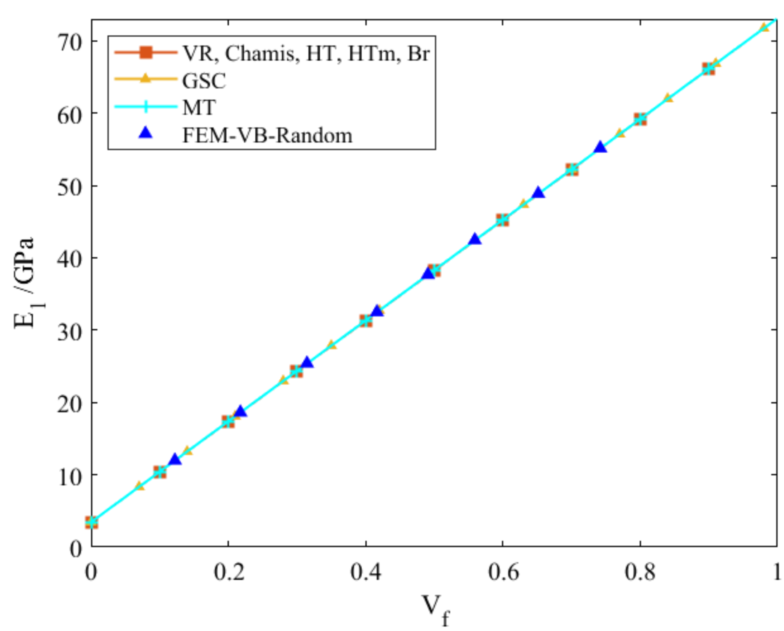

Figure 18. Comparison of micromechanics model and VB-FEM results for E_1 of a glass–epoxy composite.

For the Glass Epoxy material, the predictions for the transverse Young's modulus (E2) (Figure 19) are more scattered compared to Carbon Epoxy. While the FEM and experimental results are generally close, FEM tends to predict higher values, potentially due to the porosity of the tested composites, which is not accounted for in the numerical analysis. Additionally, differences in boundary conditions between the experiments and the numerical model may contribute to this discrepancy.

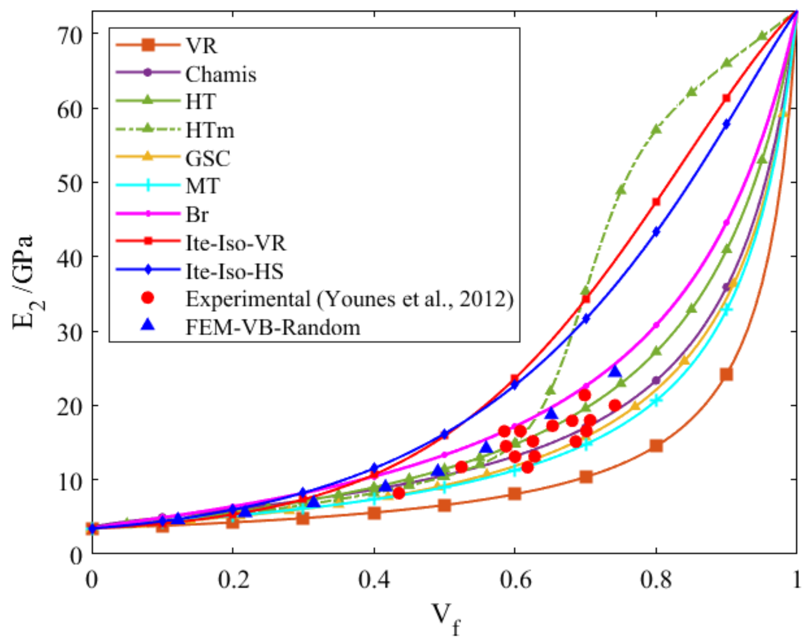

Figure 19. Comparison of micromechanics model, VB-FEM results, and experimental data for E_2 of a glass–epoxy composite [145].

For fiber volume fractions below 20%, all models demonstrate good accuracy. However, as the volume fraction increases, discrepancies become more evident. When considering the experimental data, the Voigt-Ruess model tends to predict lower values, while the iterative models predict higher values, with other models falling in between, with Chamis being the most accurate. However, when focusing on FEM data, the Bridging model appears more accurate. Given that the Bridging and Halpin-Tsai (HT) models use empirical parameters, the next most accurate model relative to FEM results is Chamis. Notably, Halpin-Tsai modified model becomes less accurate for volume fractions greater than 60%-70%.

2. Shear moduli G_{12} and G_{23}

For the Glass Epoxy material, where experimental results are not available, the longitudinal shear modulus (G_{12}) predictions (Figure 20) show that the Bridging (Br) model provides results closest to the FEM data, while the Voigt-Ruess model deviates the most.

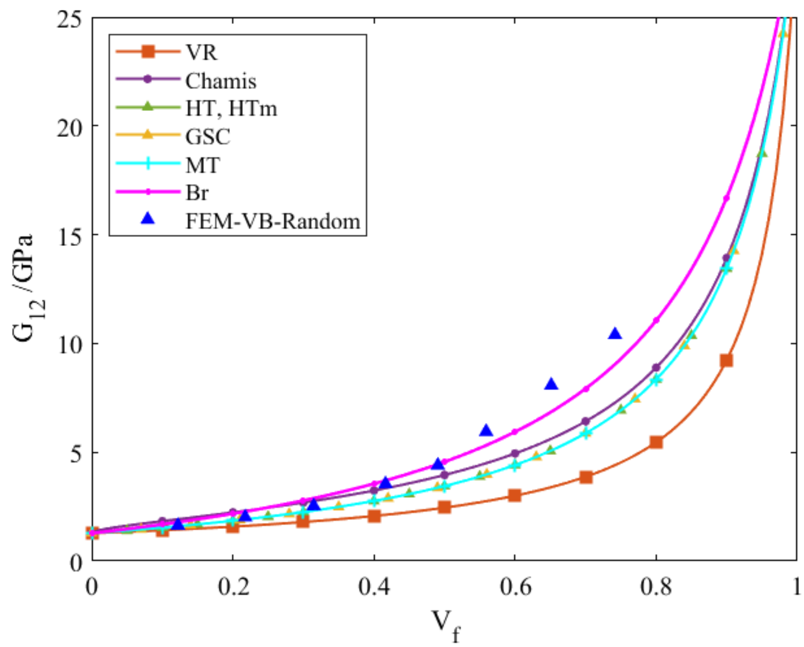

Figure 20. Comparison of micromechanics model and VB-FEM results for G_{12} of a glass–epoxy composite.

For the Glass Epoxy material, where experimental data is unavailable, the out-of-plane shear modulus predictions (Figure 21) show that the Bridging (Br) model aligns most closely with the FEM results. Considering that the Br model uses empirical parameters, the next closest model in terms of alignment with FEM data would be the Chamis model.

3. Poisson's ratio ν_{12} (see Figure 22)

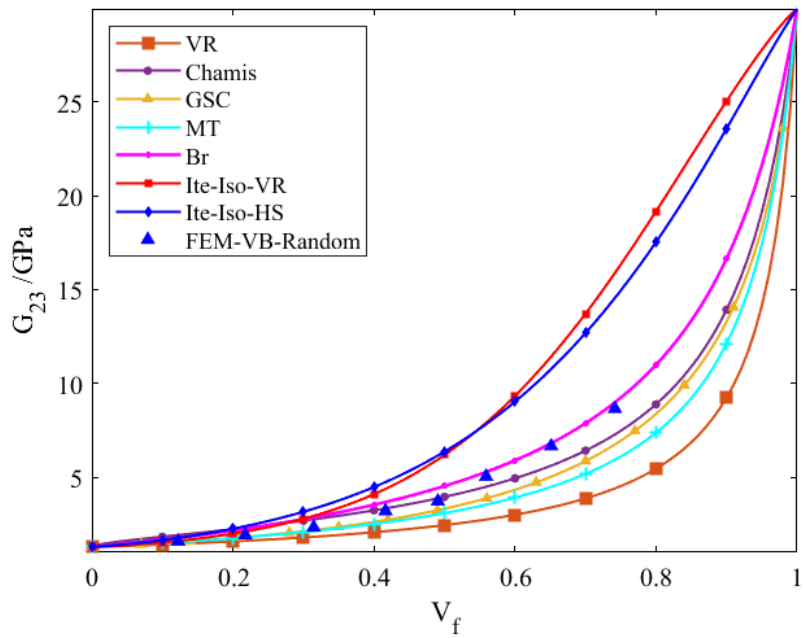

Figure 21. Comparison of micromechanics model and VB-FEM results for G_{23} of a glass–epoxy composite.

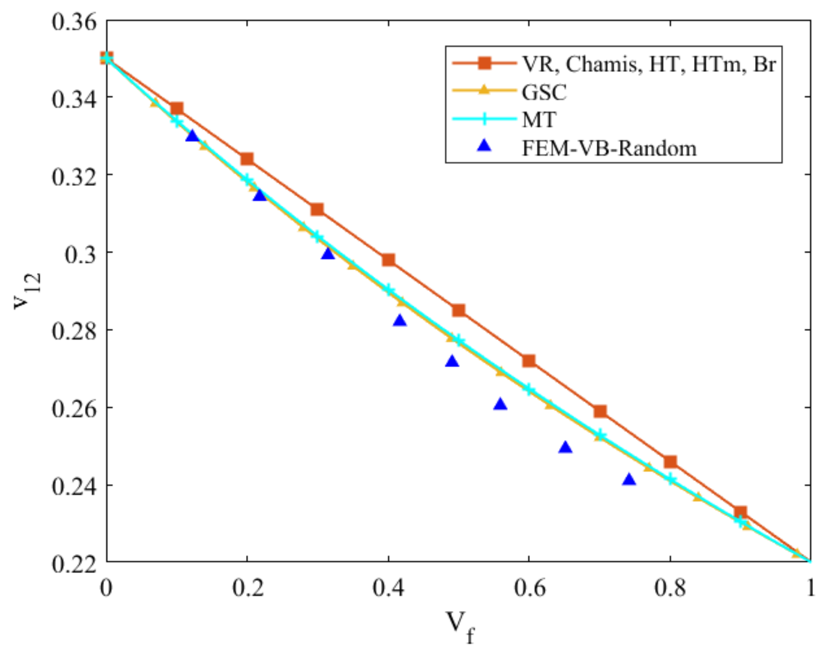

Figure 22. Comparison of micromechanics model and VB-FEM results for v_{12} of a glass–epoxy composite.

When predicting the Poisson's ratio of Glass Epoxy material (Figure 22), the MT and GSCM models match most closely with the FEM data. However, at high volume fractions, the FEM results deviate from these predictions, with the FEM results being lower.

4.2 Results Related to Laminate Plate/Shell

This section reports the effective stiffness parameters of symmetric cross-ply laminate plates using both micromechanics-based analytical predictions and voxel-based finite element modeling (VB-FEM). The stiffness predictions from FSDT are computed analytically using homogenized lamina properties derived from micromechanics models. As a result, their accuracy strongly depends on the quality of the input properties—particularly the transverse modulus E_2 and out-of-plane shear modulus G_{23}. In contrast, VB-FEM simulates the actual microstructure of the laminate, capturing local interactions and variability directly. This allows VB-FEM to provide more accurate and reliable stiffness predictions, especially when complex microstructural effects are present. First, a subset of micromechanics models capable of predicting all five independent lamina properties (E_1, E_2, G_{12}, G_{23}, and ν_{12}) is selected for input into First-Order Shear Deformation Theory (FSDT). Using these models, the in-plane stiffness matrix (A) and the transverse shear stiffness matrix (H) of the laminate are computed. The predictions are then compared with VB-FEM results and available experimental data to assess the reliability of each micromechanics model in the context of laminate-level behavior.

4.2.1 Choosing Micromechanics models

There are some factors considered to choose the most suitable micromechanics models. First, it is essential to select micromechanical models that can predict all five elastic properties—E1, E2, G12, G23, and v12. Consistency in the accurate prediction of all properties is crucial for accurate laminate behaviour prediction. Additionally, models that rely on empirical parameters can offer accurate predictions and are useful in many applications, but they should be applied with care, as their performance may depend on appropriate calibration for specific material or condition.

All micromechanical models demonstrated similar accuracy in predicting the longitudinal Young's modulus (E1) for both carbon-epoxy and glass-epoxy materials. However, when predicting Poisson's ratio (v12), GSCM and MT models provided predictions closer to numerical results than other models, although experimental data was unavailable to validate these predictions.

The Halpin-Tsai modified (HTm) model showed low accuracy in predicting E_2 at high fiber volume fractions, especially for glass-epoxy. Although the original HT model demonstrated good accuracy for glass-epoxy, it lacks the necessary formulas to predict the out-of-plane shear modulus (G23), which is crucial for laminate analysis.

Considering overall performance, GSCM and MT models stood out as the most promising candidates for predicting laminate properties, as they showed consistent accuracy across all properties. Additionally, the Bridging Model showed the closest agreement with VB-FEM results for E_2, G_{12}, and G_{23} in glass–epoxy and is selected for further analysis. However, its reliance on empirical parameters may reduce its robustness, especially when there is a large difference between the moduli of fiber and matrix phases [147]. The Chamis model also showed the second best agreement with FEM results after bridging model for glass epoxy.

In conclusion, GSCM, MT, Chamis, and Bridging Models are selected for laminate stiffness prediction due to their ability to provide all five elastic properties with good accuracy. The simpler model of Voigt–Ruess may serve as a baseline reference but is generally less reliable for critical properties like E_2 and G_{23}.

4.2.2 Validation with Experimental Data

For laminates, experimental data is typically available only for Young's moduli. To validate the finite element results, Figure 23 - Figure 26 compares experimental, VB-FEM, and analytical predictions for E_x, E_y, E_x^f, and E_y^f, using experimental data reported by Lasn et al. [58].

From Figure *23* - Figure *26*, it can be seen that, the VB-FEM results are slightly higher than the experimental data, which may be attributed to the porosity present in the tested material. Since VB-FEM simulations typically assume fully dense, defect-free materials, they may overestimate stiffness relative to experimental measurements. Among the analytical models, the Bridging Model produces predictions that most closely align with the FEM results.

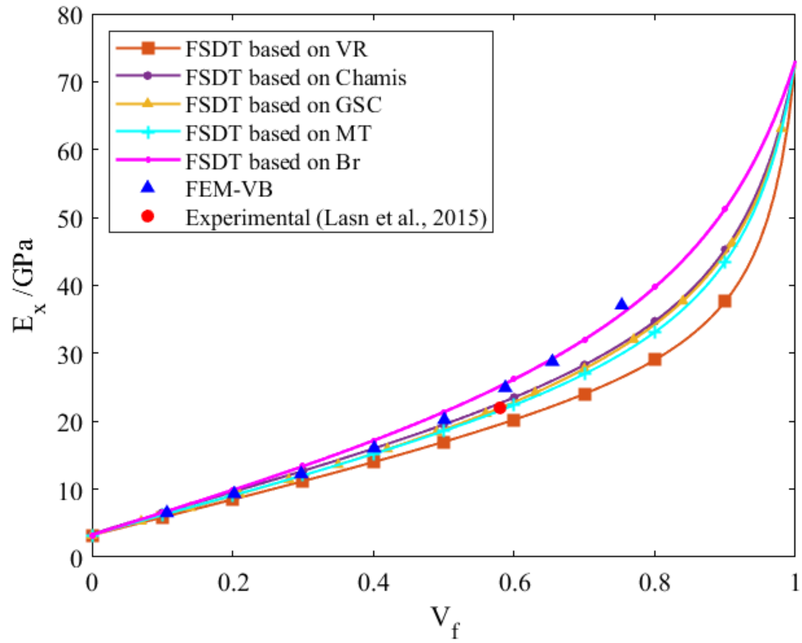

Figure 23. Comparison of predicted and experimental values of laminate Young's modulus E_x [58].

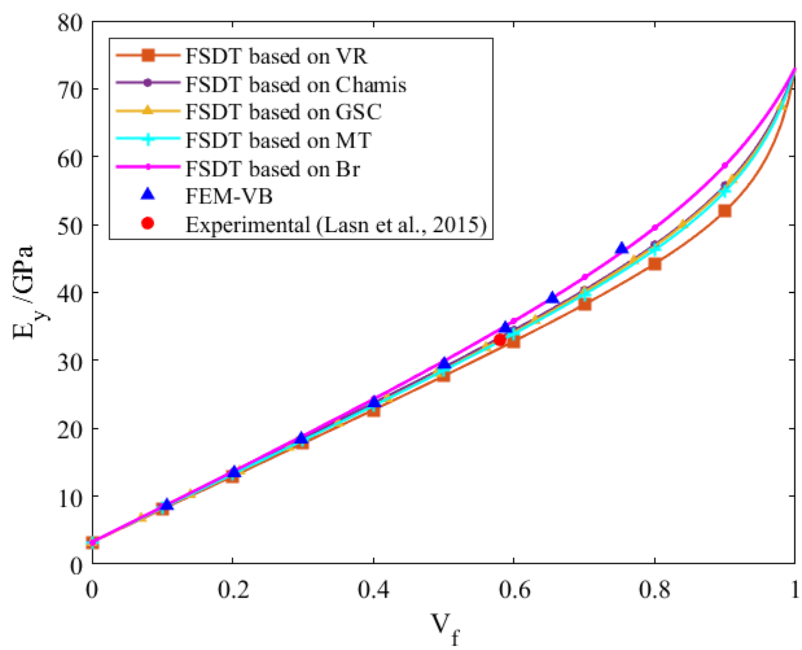

Figure 24. Comparison of predicted and experimental values of laminate Young's modulus [58].

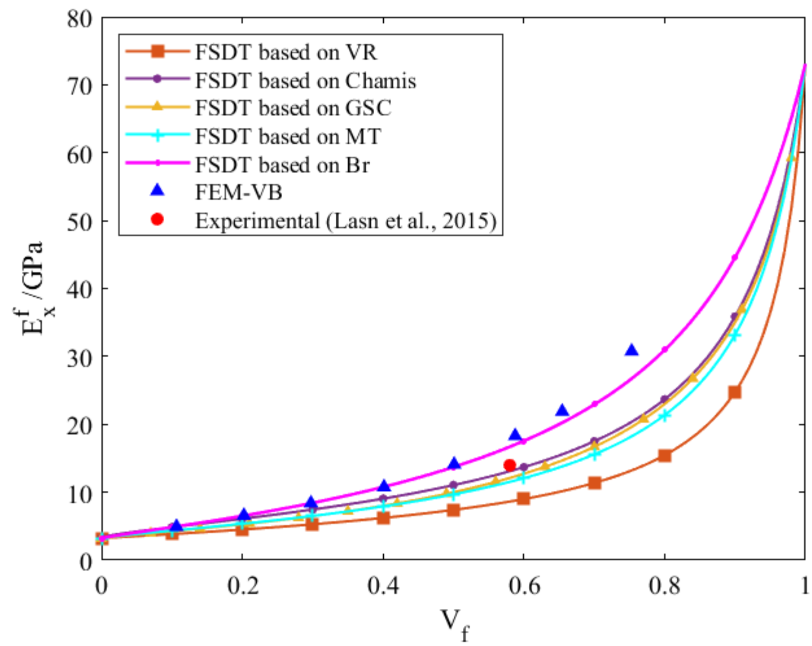

Figure 25. Comparison of predicted and experimental values of laminate Young's modulus E_x^f [58].

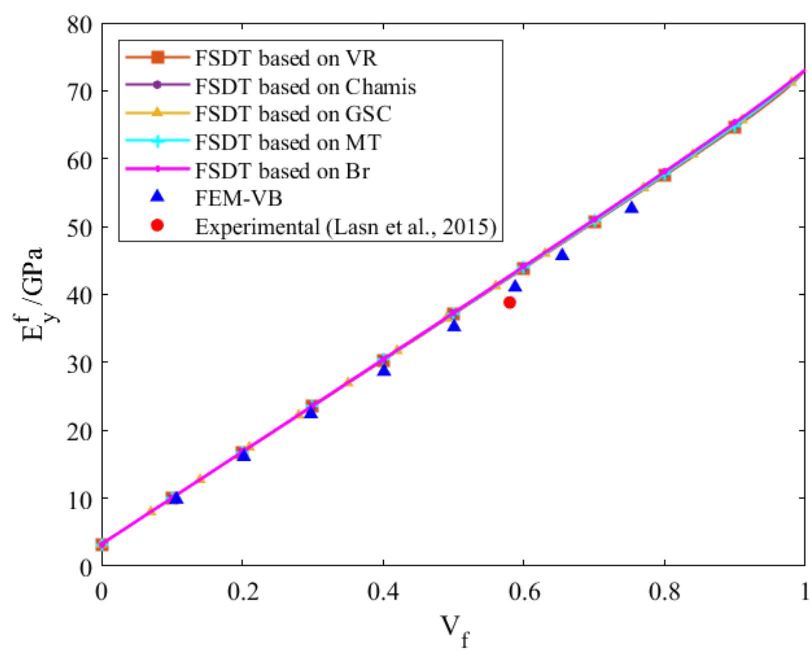

Figure 26. Comparison of predicted and experimental values of laminate Young's modulus E_y^f [58].

4.2.3 In-Plane Stiffness Matrix Parameters

Figure 27 - Figure 30 show the non-zero and independent elements of the in-plane matrix (A) as predicted by FSDT using the selected micromechanics models, alongside the corresponding VB-FEM results. These figures are discussed in the following paragraphs to highlight trends and model accuracy

The values of A(1,1) and A(2,2) depend on E_x, E_y, and ν_{xy}, with A(1,1) being more sensitive to E_x. Since E_x is influenced by the four 90° plies and two 0° plies, while E_γ is governed by the reverse stacking sequence, the higher accuracy in predicting the longitudinal modulus (E_γ) leads to better agreement for A(2,2) across all models. Overall, the Bridging Model provides the most accurate predictions for both A(1,1) and A(2,2), followed by the Chamis model, while the VR model consistently underperforms (see Figure 27 and Figure 28).

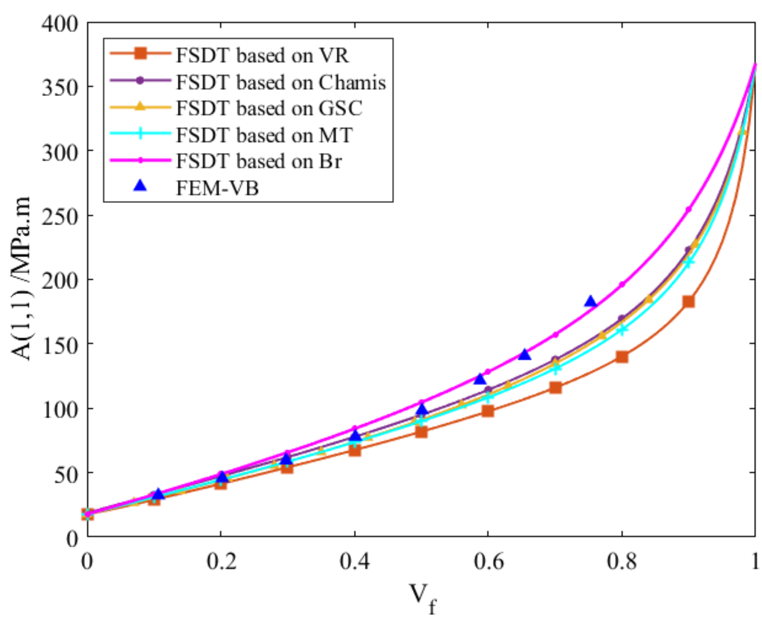

Figure 27. Comparison of A(1,1) values predicted by selected micromechanics models and VB-FEM.

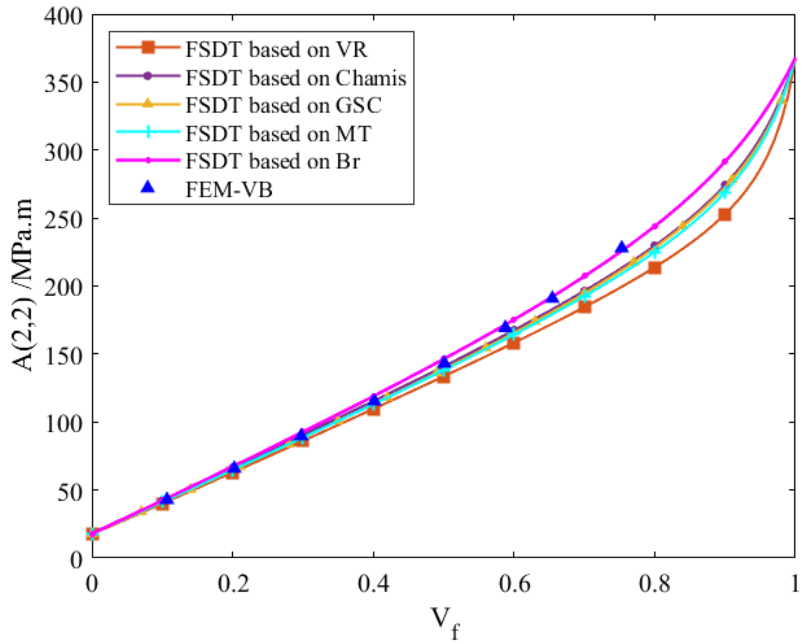

Figure 28. Comparison of A(2,2) values predicted by selected micromechanics models and VB-FEM.

For A(1,2), the FEM predictions up to a 40% fiber volume fraction closely match those from MT and GSC models. As the volume fraction increases, the FEM values approach those predicted by the Bridging Model. This trend reflects earlier findings in unidirectional composites, where ν_{12} predictions from MT and GSC aligned well with FEM, particularly at mid-range volume fractions (see Figure 29). And, the trend observed for A(3,3) mirrors that of the shear modulus in unidirectional composites. The FEM results are slightly higher than the analytical predictions but remain closest to those from the Bridging Model (see Figure 30).

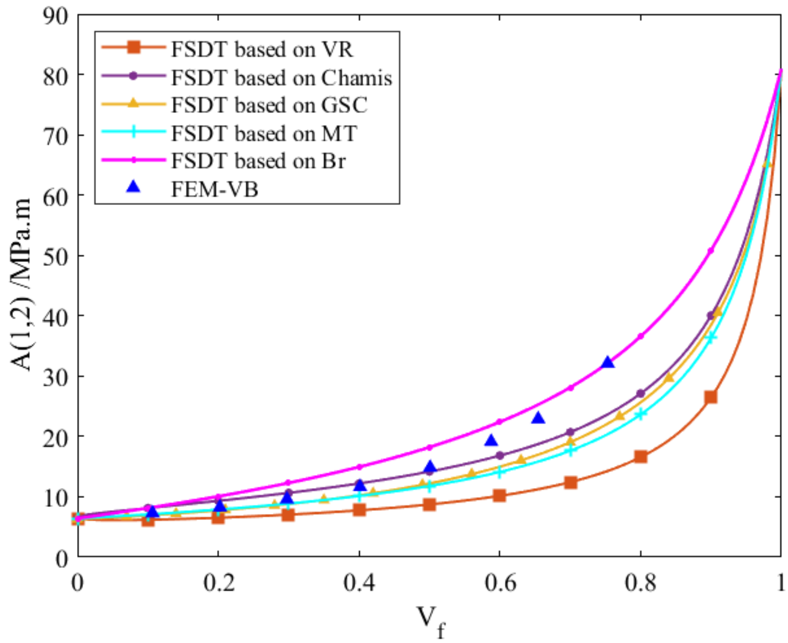

Figure 29. Comparison of A(1,2) values predicted by selected micromechanics models and VB-FEM.

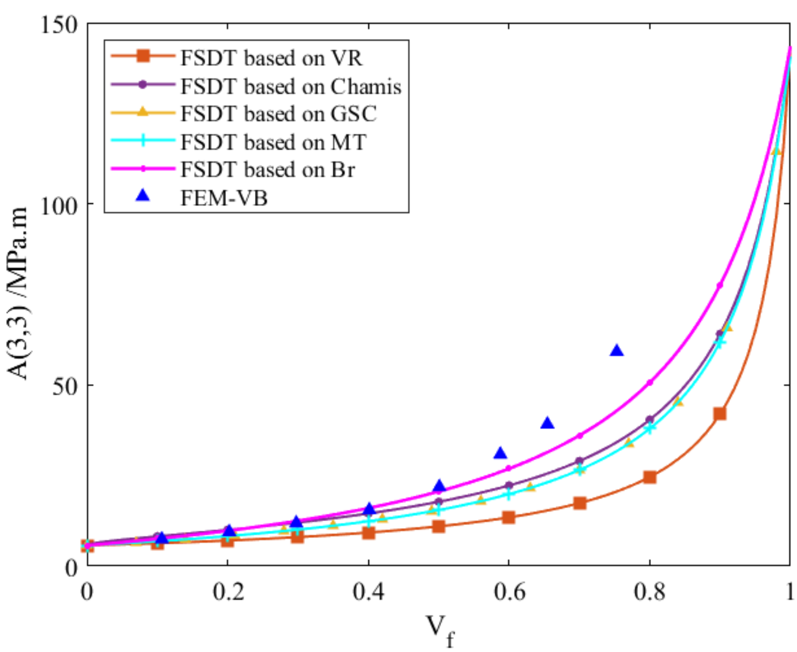

Figure 30. Comparison of A(3,3) values predicted by selected micromechanics models and VB-FEM.

4.2.4 Bending Stiffness Matrix Parameters

Figure 31 - Figure 34 present the non-zero and independent elements of the bending stiffness matrix (D) as predicted by First-Order Shear Deformation Theory (FSDT) using the selected micromechanics models, alongside corresponding results from VB-FEM. This section highlights key observations and differences in model accuracy.

The VB-FEM results for the bending stiffness matrix elements D(1,1), D(1,2), and D(2,2) are slightly higher than the corresponding predictions from the micromechanics-based models, even at a low fiber volume fraction of 0.1. Such discrepancies were not observed in the prediction of the in-plane stiffness matrix (A). The deviation originates from the estimation of Poisson's ratio υ_{xy}^{f}. During bending about the *x*-axis, efforts were made to constrain the plane at y = 100 to remain flat; however, residual warping deformation was observed, indicating incomplete constraint enforcement. This directly affected the computed value of υ_{xy}^{f}, which in turn influenced the accuracy of D(1,1), D(1,2), and D(2,2), while leaving D(3,3) unaffected (see Figure 31 - Figure 34).

D(2,2) is more sensitive to E_{y}^{f}, which is primarily influenced by the stiffness of the 0° plies located at the outermost layers of the laminate during bending about the *y*-axis. As a result, D(2,2) exhibits a nearly linear trend with increasing fiber volume fraction. In contrast, D(1,1) is governed by E_{x}^{f}, associated with the 90° plies, and shows a less linear response (see Figure 31 and Figure 32).

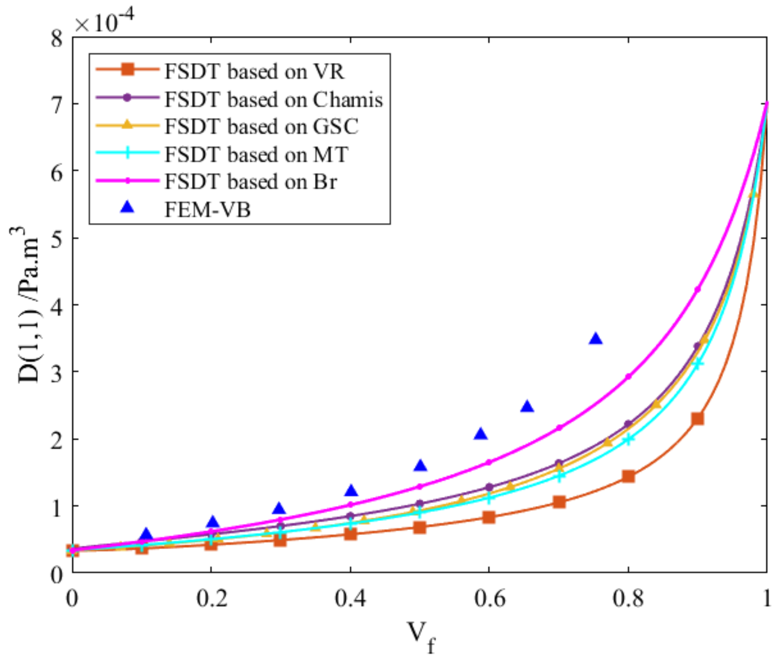

Figure 31. Comparison of D(1,1) values predicted by selected micromechanics models and VB-FEM.

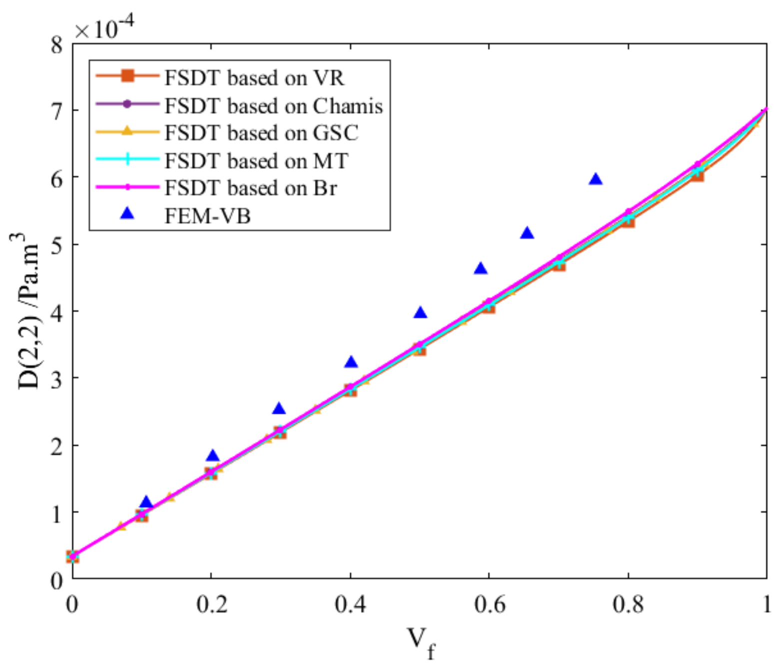

Figure 32. Comparison of D(2,2) values predicted by selected micromechanics models and VB-FEM.

In the absence of the deviation caused by the inaccurate estimation of υ_{xy}^{f}, the trend for D(1,2) would have followed a similar pattern to that observed for A(1,2). In that case, the VB-FEM results would align with the predictions from the Mori–Tanaka (MT) and Generalized Self-Consistent (GSC) models at low to mid fiber volume fractions and approach the Bridging Model at higher volume fractions (see Figure 33). The element D(3,3) closely follows the trend of the in-plane stiffness term A(3,3) and the shear modulus G_{12}, consistent with the behavior observed in the unidirectional composite analysis (see Figure 34).

4.2.5 Transverse Shear Stiffness Matrix Parameters

Figure 35 and Figure 36 illustrates the non-zero elements of the transverse shear stiffness matrix (H) as predicted by both analytical models and VB-FEM simulations. The components are examined below to evaluate the predictive performance of the models under transverse shear conditions.

In examining the transverse shear properties, the FEM results for H(1,1) and H(2,2) are generally similar; however, at higher fiber volume fractions, H(1,1) shows slightly better agreement with the analytical predictions. The element H(1,1) is directly related to the shear modulus G_{yz}. Under transverse shear loading, the central region of the laminate primarily carries the shear force. Since the central layers are oriented at 0°, the effective shear modulus in the y–z plane corresponds to G_{23} of a unidirectional lamina. As observed in the unidirectional analysis, predictions for G_{23} align more closely with analytical models than those for G_{12}, which helps explain the improved agreement of H(1,1) relative to H(2,2) (see Figure 35 and Figure 36).

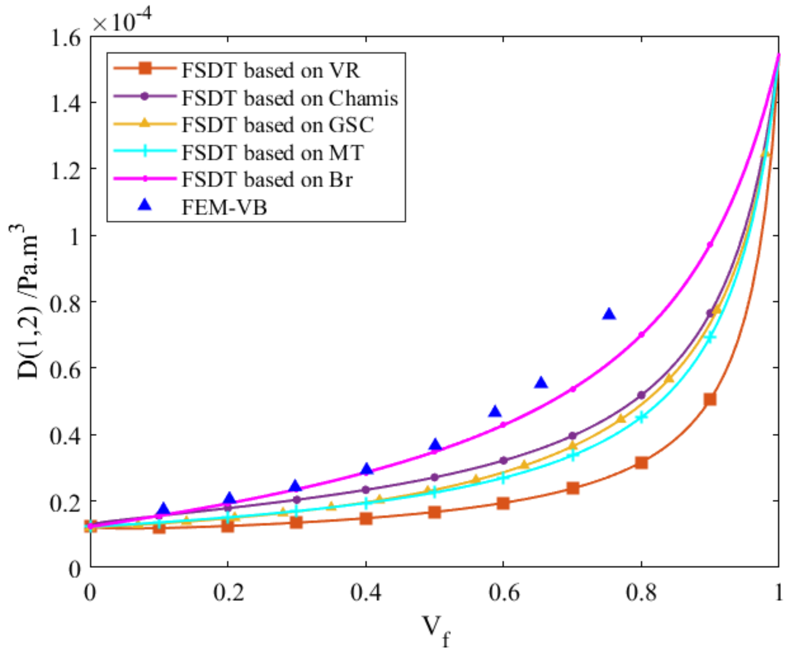

Figure 33. Comparison of D(1,2) values predicted by selected micromechanics models and VB-FEM.

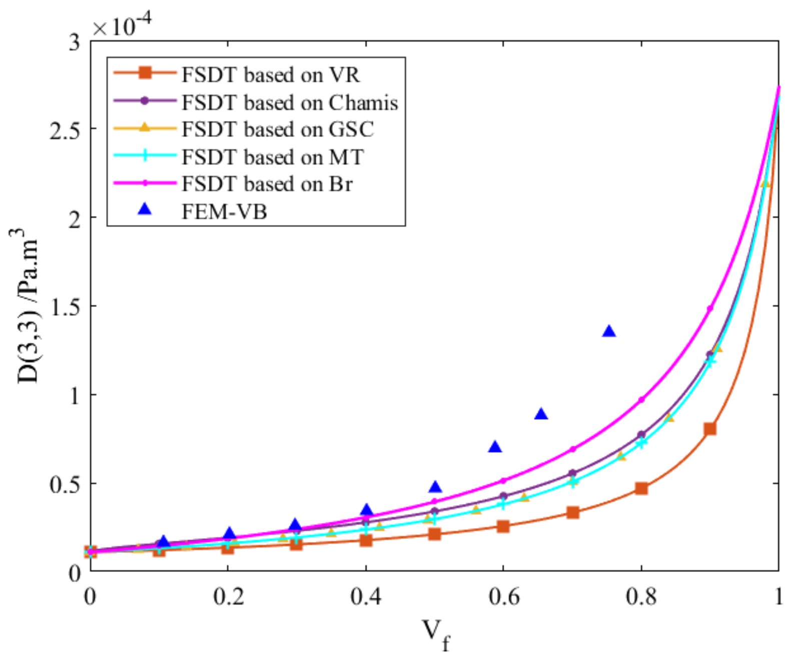

Figure 34. Comparison of D(3,3) values predicted by selected micromechanics models and VB-FEM.

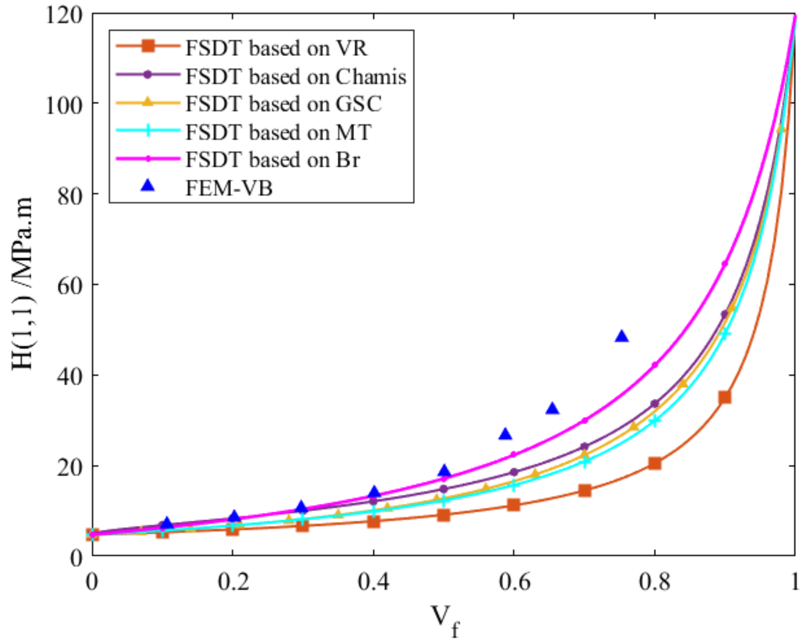

Figure 35. Comparison of H(1,1) values predicted by selected micromechanics models and VB-FEM.

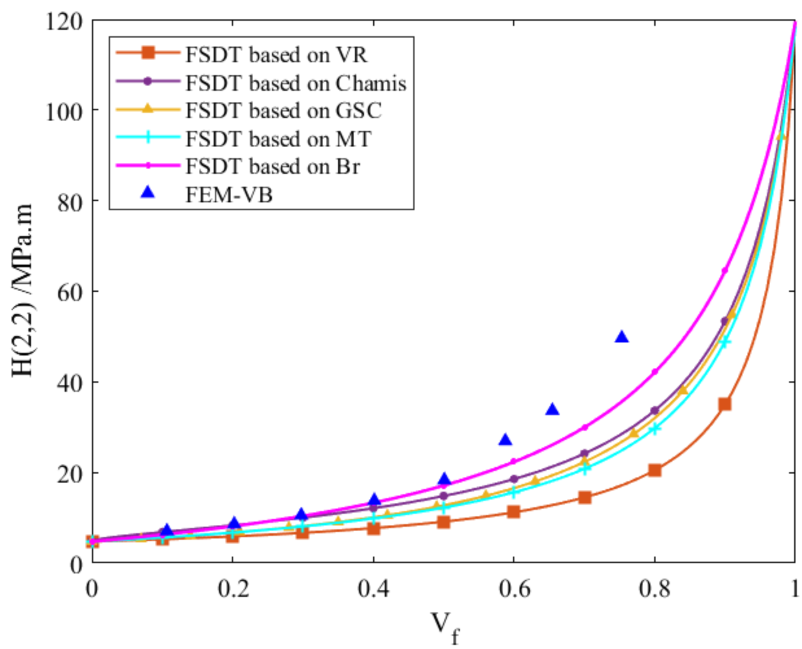

Figure 36. Comparison of H(2,2) values predicted by selected micromechanics models and VB-FEM.

4.3 Discussion of Results

This section provides a detailed interpretation of the findings presented in Sections 4.1 and 4.2, focusing on the accuracy and limitations of micromechanics models in predicting the elastic properties of unidirectional and laminate composites. The first part discusses how the assumptions embedded in each micromechanics model affect their performance, particularly in relation to fiber–matrix property contrast and fiber volume fraction. The second part explores the implications of these lamina-level predictions on laminate plate and shell stiffness, highlighting the propagation of micromechanical errors into global laminate behavior.

4.3.1 Unidirectional Fiber Composite

The results for unidirectional composites demonstrate that while all micromechanics models predict the longitudinal Young's modulus (E_1) with high accuracy, their performance varies significantly for the other elastic constants—particularly the transverse modulus (E_2) and the in-plane and out-of-plane shear moduli (G_{12} and G_{23}). These variations stem from the assumptions embedded in each model. For example, the Voigt-Reuss model, which serves as a basic reference, relies on iso-strain and iso-stress assumptions in its Voigt and Reuss formulations, respectively. The iso-stress condition results in poor accuracy when predicting transverse and shear properties.

The influence of contrast between constituent properties on model accuracy is apparent when comparing carbon-epoxy and glass-epoxy systems. In carbon-epoxy composites, where the contrast between matrix and fiber properties is relatively low in the transverse direction, most models perform reasonably well across all moduli. However, in glass-epoxy, the higher contrast leads to greater deviations.

At low fiber volume fractions, most models show acceptable agreement with VB-FEM results for both materials, although the Chamis model notably underperforms in the carbon-epoxy case. For glass-epoxy, where prediction errors are generally more pronounced, the Bridging model demonstrates enhanced accuracy at high volume fractions. The Halpin–Tsai model offers good agreement for E_2 in this material. Meanwhile, the Generalized Self-Consistent (GSC), Mori–Tanaka (MT), and Chamis models show close alignment with FEM results at low to mid volume fractions.

Models such as Halpin–Tsai and Bridging introduce fitting parameters to better capture the influence of fiber packing and geometric effects. The Bridging model, in particular, shows the most consistent agreement with FEM predictions for E_2, G_{12}, and G_{23}—even at high fiber volume fractions. However, the reliability of this model depends on appropriate selection of bridging parameters, which may vary depending on the material properties.
Iterative models, including Iter-Iso-VR and Iter-Iso-HS, yield accurate results for carbon-epoxy composites and outperform classical models at certain volume fractions. However, for glass-epoxy composites, these models do not surpass more established approaches in predictive accuracy, though they may still offer value under specific conditions or with further development.

4.3.2 Cross-Ply Laminate Composite

The accuracy of laminate stiffness predictions depends critically on the quality of the underlying lamina properties. Since micromechanics models often exhibit reduced accuracy—particularly in high volume fractions and systems with high stiffness contrast between fiber and matrix phases—these inaccuracies can propagate through lamination theory and lead to cumulative errors in the global stiffness matrices. Consequently, to reliably predict laminate stiffness, a micromechanics model must provide accurate estimates for all five elastic constants of the lamina: E_1, E_2, G_{12}, G_{23}, and ν_{12}.

Since the differences among micromechanics model predictions for carbon-epoxy were small—particularly in the transverse and shear properties—laminate-level comparisons were focused on glass-epoxy composites, where the contrast in constituent properties leads to more pronounced deviations. To evaluate the models' performance in predicting laminate stiffness, the ten non-zero elements of in-plane stiffness matrix (A), bending stiffness matrix (D), and transverse shear stiffness matrix (H) for a symmetric cross-ply glass-epoxy laminate are presented.

Experimental data for laminate composites are often limited and rarely include all stiffness parameters. For the glass/epoxy cross-ply laminate examined in this work, in-plane and flexural moduli reported by Lasn et al. [58] are used to validate the VB-FEM results. As expected, VB-FEM predictions are slightly higher than experimental values, likely due to the absence of porosity in the numerical model. However, VB-FEM predictions showed noticeably better agreement with experimental data for the flexural modulus (Figure *25* and Figure *26*). Given the unavailability of complete experimental data, VB-FEM results are adopted as the reference for evaluating the ADH matrices in this study.

As shown in the results presented in Sections 4.2.3-4.2.5, trends in the laminate stiffness matrix elements reflect those observed in the unidirectional composite properties. This suggests that the accuracy of the micromechanical predictions at the lamina level has a direct impact on laminate-level behavior. In particular, inaccuracies in even one of the five independent elastic properties can distort multiple entries of the laminate stiffness matrices. Among all models examined, the Bridging Model consistently provided the most accurate predictions relative to VB-FEM results (Figure *27*-Figure 36). However, its reliability depends on the proper selection of two empirical Bridging parameters, which can significantly influence results—especially for composites with large disparities between fiber and matrix properties (e.g., modulus mismatch).

Chapter 5

Conclusion and Future Work

This thesis evaluated the accuracy of various micromechanics models in predicting the five independent elastic constants of unidirectional fiber-reinforced composites and assessed how these predictions influence the laminate stiffness properties derived using First-Order Shear Deformation Theory (FSDT). A high-fidelity voxel-based finite element modeling (VB-FEM) approach was developed and used as a numerical benchmark. Comparisons were also made with available experimental data to validate the findings.

5.1 Summary of Findings

1. For unidirectional composites, the transverse Young's modulus (E_2) and shear moduli (G_{12}, G_{23}) are more sensitive to microstructural characteristics than the longitudinal modulus (E_1). Nearly all micromechanics models accurately predicted E_1, but substantial discrepancies were observed for E_2, G_{12}, and G_{23}.
2. The Bridging model demonstrated the most consistent agreement with VB-FEM across all five properties of unidirectional composites, particularly for glass-epoxy material at higher fiber volume fractions.

3. The study highlighted that model accuracy diminishes as the modulus contrast between fiber and matrix increases, with glass-epoxy composites presenting a greater challenge for analytical predictions than carbon-epoxy systems.
4. For laminate stiffness predictions, discrepancies in lamina-level input properties were shown to propagate to the laminate scale, affecting the ten non-zero stiffness matrix components of the modeled symmetric cross-ply laminate. The Bridging model again showed the best performance, while Voigt–Reuss model underperformed.
5. The voxel-based finite element modeling (VB-FEM) framework developed in this study served as a high-fidelity numerical approach for evaluating composite stiffness properties. While not a substitute for experimental validation, it provided a consistent and detailed reference for assessing the accuracy of micromechanics models, particularly in capturing the influence of fiber arrangement and property contrast. Its application to both unidirectional and laminate cases demonstrated its usefulness as a comparative tool for model evaluation.

5.2 Contributions to the Field

The primary contribution of this research lies in its systematic and comparative assessment of micromechanics models using VB-FEM. First, assessing the model's performance in predicting unidirectional lamina properties and using the more accurate and comprehensive one to be used for laminate stiffness matrices of symmetric cross-ply laminate. In order to demonstrate the link and similarities between the trends in these levels. Discussing how prediction errors at the lamina level affect laminate-level stiffness estimations.

The broader impact of this work lies in guiding researchers and engineers in selecting appropriate micromechanics models based on material type, fiber volume fraction, and property of interest. The VB-FEM models developed here offer a reliable numerical reference for future studies seeking to validate or refine analytical predictions in composite laminates.

Additionally, this thesis provides novel insight into the applicability of iterative isotropization models—which were originally developed for isotropic particulate composites—to transversely isotropic fiber-reinforced systems. Their performance, particularly in predicting transverse and shear moduli for carbon-epoxy, suggests potential.

5.3 Limitations of the Study and Recommendations for Future Research

It should be noted that several of the micromechanics models used in this study, including Mori–Tanaka, Generalized Self-Consistent, and the iterative isotropized models (Iter-Iso-VR, Iter-Iso-HS), are empirical or semi-empirical in nature. While these models are widely adopted due to their simplicity and reasonable predictive performance, they are not derived from first-principle variational formulations. As such, they do not fully reflect the theoretical rigor offered by approaches grounded in the theory of composites and variational methods [148–150]. In this work, our focus was on evaluating practical accuracy for laminate stiffness prediction rather than conducting a formal theoretical analysis. Nevertheless, the incorporation of more theoretically grounded models remains an important direction for future research, particularly in applications where rigorous bounds or optimality criteria are essential.

In the FEM model used in this study, the term “random composite” refers to a single realization of fiber distributions generated using a non-overlapping random sequential algorithm. This approach captures geometric randomness associated with manufacturing variability but does not represent a statistical ensemble or invoke a formal probability distribution. As such, it provides a practical but limited representation of randomness. While the use of a single RVE is common for computational efficiency and qualitative comparison, it may not fully capture the statistical variability of composite behavior, as addressed in more rigorous stochastic frameworks [148–150]. Future studies could incorporate ensembles of RVEs or structural sum-based descriptors to better capture statistical effects in composite microstructures.

Despite its advantages, the voxel-based FEM approach also has limitations that should be acknowledged. One limitation is that it is computationally intensive, especially for high-resolution models or when simulating large-scale laminate structures. Additionally, the voxelization process leads to a stair-step approximation of curved fiber–matrix interfaces, which may reduce geometric fidelity and affect the accuracy of local stress predictions. These trade-offs must be considered when applying this method to composites with complex geometries or when high precision is required.

Another limitation is related to the scope of the laminate configurations studied. The analysis was limited to a single symmetric cross-ply stacking sequence ([90/90/0/0/90/90]), which, although representative, does not cover the full range of practical laminate configurations such as angle-ply, quasi-isotropic, or hybrid laminates. Extending the analysis to these configurations could help generalize the findings and further evaluate the micromechanics models under more diverse loading and geometric conditions.

The study also relies on limited experimental datasets. While experimental data were used to validate VB-FEM predictions for both unidirectional and laminate composites, complete elastic property data for all five stiffness parameters are were not available in literature and for the availability of experimental data for laminate level were even less. This constraint necessitated the use of VB-FEM as a surrogate reference in some cases.

Considering the limitations, while the Bridging Model appears promising, further experimental validation is necessary to confirm its robustness across different material systems and loading conditions. Moreover, although this study focused on symmetric cross-ply laminates, extending the methodology to other laminate configurations (e.g., angle-ply, quasi-isotropic) would offer broader insights into model applicability.

Bibliography

[1] F. Rubino, A. Nisticò, F. Tucci, P. Carlone, Marine Application of Fiber Reinforced Composites: A Review, J Mar Sci Eng 8 (2020). https://doi.org/10.3390/jmse8010026.

[2] V.M. Karbhari, L. Zhao, Use of composites for 21st century civil infrastructure, Comput Methods Appl Mech Eng 185 (2000) 433–454. https://doi.org/https://doi.org/10.1016/S0045-7825(99)90270-0.

[3] M.S.H. Al-Furjan, L. Shan, X. Shen, M.S. Zarei, M.H. Hajmohammad, R. Kolahchi, A review on fabrication techniques and tensile properties of glass, carbon, and Kevlar fiber reinforced rolymer composites, Journal of Materials Research and Technology 19 (2022) 2930–2959. https://doi.org/https://doi.org/10.1016/j.jmrt.2022.06.008.

[4] A.R. Melro, P.P. Camanho, S.T. Pinho, Influence of geometrical parameters on the elastic response of unidirectional composite materials, Compos Struct 94 (2012). https://doi.org/10.1016/j.compstruct.2012.05.004.

[5] E. Carrera, Theories and finite elements for multilayered, anisotropic, composite plates and shells, Archives of Computational Methods in Engineering 9 (2002) 87–140. https://doi.org/10.1007/BF02736649.

[6] A. Hallal, R. Younes, F. Fardoun, Review and comparative study of analytical modeling for the elastic properties of textile composites, Compos B Eng 50 (2013) 22–31. https://doi.org/10.1016/J.COMPOSITESB.2013.01.024.

[7] Y. Ueki, H. Lilholt, B. Madsen, Experimental evaluation of stiffness predictions of multiaxial flax fibre composites by classical laminate theory, PLoS One 15 (2020). https://doi.org/10.1371/journal.pone.0234701.

[8] Z.-M. Huang, Y.-X. Zhou, Strength of Fibrous Composites, 1. Aufl., Springer-Verlag, Berlin, Heidelberg, 2011.

[9] Y.-C. Wang, Z.-M. Huang, A new approach to a bridging tensor, Polym Compos 36 (2015) 1417–1431. https://doi.org/10.1002/pc.23048.

[10] L.L. Vignoli, M.A. Savi, P.M.C.L. Pacheco, A.L. Kalamkarov, Micromechanical analysis of transversal strength of composite laminae, Compos Struct 250 (2020) 112546. https://doi.org/10.1016/J.COMPSTRUCT.2020.112546.

[11] L.L. Vignoli, M.A. Savi, P.M.C.L. Pacheco, A.L. Kalamkarov, Comparative analysis of micromechanical models for the elastic composite laminae, Compos B Eng 174 (2019) 106961. https://doi.org/10.1016/J.COMPOSITESB.2019.106961.

[12] M. Heidari-Rarani, K. Bashandeh-Khodaei-Naeini, S.M. Mirkhalaf, Micromechanical modeling of the mechanical behavior of unidirectional composites – A comparative study, Journal of Reinforced Plastics and Composites 37 (2018) 1051–1071. https://doi.org/10.1177/0731684418779441.

[13] R.M. Jones, Mechanics of composite materials, Second edi, CRC Press, 2018.

[14] A.K.. Kaw, Mechanics of composite materials, Taylor & Francis, 2006.

[15] M. W.Hyer, Stress Analysis of Fiber-Reinforced Composite Materials, McGraw-Hill Science/Engineering/Math (1998) 627.

[16] P.K. Mallick, Fiber-reinforced composites : materials, manufacturing, and design, Third edit, CRC Press, Taylor & Francis Group, Boca Raton, FL, 2007. https://doi.org/10.1201/9781420005981.

[17] E.J. Barbero, Finite element analysis of composite materials using ANSYS, Second edi, CRC Press, Taylor & Francis Group, Boca Raton, 2014.

[18] M. Yüksekkaya, T. Howard, S. Adanur, Influence of the fabric properties on fabric stiffness for the industrial fabrics, Textile and Apparel (2008) 263--267. https://www.researchgate.net/publication/267233556 (accessed July 16, 2025).

[19] A. Wongsto, S. Li, Micromechanical FE analysis of UD fibre-reinforced composites with fibres distributed at random over the transverse cross-section, Compos Part A Appl Sci Manuf 36 (2005) 1246–1266. https://doi.org/10.1016/J.COMPOSITESA.2005.01.010.

[20] R.O. Ogunleye, S. Rusnakova, M. Zaludek, S. Emebu, The Influence of Ply Stacking Sequence on Mechanical Properties of Carbon/Epoxy Composite Laminates, Polymers (Basel) 14 (2022). https://doi.org/10.3390/POLYM14245566.

[21] M.A. Caminero, G.P. Rodríguez, J.M. Chacón, I. García-Moreno, Tensile and flexural damage response of symmetric angle-ply carbon fiber-reinforced epoxy laminates: Non-linear response and effects of thickness and ply-stacking sequence, Polym Compos 40 (2019) 3678–3690. https://doi.org/10.1002/PC.25230.

[22] A. Mlyniec, J. Korta, R. Kudelski, T. Uhl, The influence of the laminate thickness, stacking sequence and thermal aging on the static and dynamic behavior of

carbon/epoxy composites, Compos Struct 118 (2014) 208–216. https://doi.org/10.1016/J.COMPSTRUCT.2014.07.047.

[23] K. Grigoriou, A.P. Mouritz, Influence of ply stacking pattern on the structural properties of quasi-isotropic carbon-epoxy laminates in fire, Compos Part A Appl Sci Manuf 99 (2017) 113–120. https://doi.org/10.1016/J.COMPOSITESA.2017.04.008.

[24] A. Parmiggiani, M. Prato, M. Pizzorni, Effect of the fiber orientation on the tensile and flexural behavior of continuous carbon fiber composites made via fused filament fabrication, International Journal of Advanced Manufacturing Technology 114 (2021) 2085–2101. https://doi.org/10.1007/S00170-021-06997-5.

[25] Y. Su, D. Zhang, X. Gong, M. Shen, Mechanical behavior in bending deformation of thermoplastic composite laminates with different stacking sequences, J Compos Mater 50 (2016) 1037–1048. https://doi.org/10.1177/0021998315586863.

[26] K. Mizumoto, Y. Kanda, T. Isaki, K. Sanada, K. Nagata, A. Miyata, K. Fujihara, Effect of fiber orientation on the tensile properties of cross-ply laminates of PP reinforced continuous carbon fiber, J Compos Mater 55 (2021) 3483–3491. https://doi.org/10.1177/00219983211015720.

[27] S. mahboubizadeh, A. Sadeq, Z. Arzaqi, O. Ashkani, M. Samadoghli, Advancements in fiber-reinforced polymer (FRP) composites: an extensive review, Discover Materials 4 (2024). https://doi.org/10.1007/S43939-024-00091-9.

[28] K. Mohamed, J.A. Abdalla, R.A. Hawileh, A.E.S. Musa, Use of bore-epoxy anchorage system with CFRP laminates for shear strengthening of RC beams: An

experimental and analytical investigation, Structures (Oxford) 70 (2024) 107676-. https://doi.org/10.1016/j.istruc.2024.107676.

[29] M. AlMuhanna, R. AlSenan, E. Mustafaraj, E. Luga, M. Corradi, Fibre reinforcement of cement mortars for reinforcement of masonry buildings: an experimental investigation, Journal of Building Pathology and Rehabilitation 9 (2024).

[30] N. Khodadadi, H. Roghani, E. Harati, M. Mirdarsoltany, F. De Caso, A. Nanni, Fiber-reinforced polymer (FRP) in concrete: A comprehensive survey, Constr Build Mater 432 (2024). https://doi.org/10.1016/j.conbuildmat.2024.136634.

[31] Mohammed Yusuf, Oluseyi Salami, Wasiu O. Amusat, Advances in carbon-fiber reinforced polymers and composites for sustainable concrete structures, World Journal of Advanced Research and Reviews 23 (2024) 2308–2330. https://doi.org/10.30574/wjarr.2024.23.2.2601.

[32] M.M. Alzahrani, K.A. Alamry, M.A. Hussein, Recent advances of Fiber-reinforced polymer composites for defense innovations, Results Chem 15 (2025) 102199-.

[33] E.C. Tsirogiannis, E. Daskalakis, M.H. Hassan, A.M. Omar, P. Bartolo, Ballistic design and testing of a composite armour reinforced by CNTs suitable for armoured vehicles, Defence Technology 32 (2024) 173–195. https://doi.org/10.1016/j.dt.2023.04.013.

[34] A. Bhat, J. Naveen, M. Jawaid, M.N.F. Norrrahim, A. Rashedi, A. Khan, Advancement in fiber reinforced polymer, metal alloys and multi-layered armour systems for ballistic applications – A review, Journal of Materials Research and Technology 15 (2021) 1300–1317.

[35] V. Kadlag, A. Hire, A review on applications of fiber reinforced polymer composite in automotive industry, Int J Adv Res Electr Electron Instrum Eng 6 (2017) 3726–3729.

[36] G. Marmol, D.P. Ferreira, R. Fangueiro, Automotive and construction applications of fiber reinforced composites, Fiber Reinforced Composites: Constituents, Compatibility, Perspectives and Applications (2021) 785–819. https://doi.org/10.1016/B978-0-12-821090-1.00009-0.

[37] Y. Lin, J. Min, H. Teng, J. Lin, J. Hu, N. Xu, Flexural performance of steel–FRP composites for automotive applications, SpringerY Lin, J Min, H Teng, J Lin, J Hu, N XuAutomotive Innovation, 2020•Springer 3 (2020) 280–295. https://doi.org/10.1007/S42154-020-00109-X.

[38] A. Hallal, A. Elmarakbi, A. Shaito, H. El-Hage, Overview of Composite Materials and Their Automotive Applications, Advanced Composite Materials for Automotive Applications: Structural Integrity and Crashworthiness (2013) 3–28. https://doi.org/10.1002/9781118535288.CH1.

[39] D. Getu, R.B. Nallamothu, M. Masresha, S.K. Nallamothu, A.K. Nallamothu, Production and characterization of bamboo and sisal fiber reinforced hybrid composite for interior automotive body application, Mater Today Proc 38 (2021) 2853–2860.

[40] W. Zhang, J. Xu, Advanced lightweight materials for Automobiles: A review, Mater Des 221 (2022) 110994-. https://doi.org/10.1016/j.matdes.2022.110994.

[41] J.N. Reddy, Mechanics of Laminated Composite Plates and Shells: Theory and Analysis, 2nd ed., CRC Press, 2003.

[42] W. Voigt, Ueber die Beziehung zwischen den beiden Elasticitätsconstanten isotroper Körper, Ann Phys 274 (1889) 573–587. http://dx.doi.org/10.1002/andp.18892741206.

[43] A. Reuß, Berechnung der fließgrenze von mischkristallen auf grund der plastizitäts-bedingung für einkristalle., ZAMM-Journal of Applied Mathematics and Mechanics/Zeitschrift Für Angewandte Mathematik Und Mechanik 9 (1929) 49–58. http://dx.doi.org/10.1002/zamm.19290090104.

[44] G. Kou, W. Zhang, J. Chen, J. Chen, Z. Yang, An improved rule of mixture model based on deformation coordination in predicting engineering constants of unidirectional fiber reinforced composites, Mater Today Commun 34 (2023) 105072-.

[45] Z. Hashin, S. Shtrikman, A variational approach to the theory of the elastic behaviour of multiphase materials, J Mech Phys Solids 11 (1962). https://doi.org/10.1016/0022-5096(63)90060-7.

[46] C.C. Chamis, Simplified composite micromechanics equations for hygral, thermal and mechanical properties, (1983). https://ntrs.nasa.gov/citations/19830011546.

[47] J.C. Halpin, Effects of Environmental Factors on Composite Materials, Air Force technical report. AFML-TR-67-423, (1969). https://apps.dtic.mil/sti/tr/pdf/ADA306357.

[48] R.L. Hewitt, M.C. De Malherbe, An Approximation for the Longitudinal Shear Modulus of Continuous Fibre Composites, J Compos Mater 4 (1970) 280–282. https://doi.org/10.1177/002199837000400214.

[49] E. Giner, A. Vercher, M. Marco, C. Arango, Estimation of the reinforcement factor xi for calculating the transverse stiffness E-2 with the Halpin-Tsai equations using

the finite element method, Compos Struct 124 (2015) 402–408. https://doi.org/10.1016/j.compstruct.2015.01.008.

[50] Z. Hashin, B.W. Rosen, The Elastic Moduli of Fiber-Reinforced Materials, J Appl Mech 31 (1964) 223–232. https://doi.org/10.1115/1.3629590.

[51] Z. Hashin, On elastic behaviour of fibre reinforced materials of arbitrary transverse phase geometry, J Mech Phys Solids 13 (1965) 119–134. https://doi.org/10.1016/0022-5096(65)90015-3.

[52] R.M. Christensen, K.H. Lo, Solutions for effective shear properties in three phase sphere and cylinder models, J Mech Phys Solids 27 (1979) 315–330. https://doi.org/10.1016/0022-5096(79)90032-2.

[53] T. Mori, K. Tanaka, Average stress in matrix and average elastic energy of materials with misfitting inclusions, Acta Metallurgica 21 (1973) 571–574. https://doi.org/10.1016/0001-6160(73)90064-3.

[54] Y. Benveniste, A new approach to the application of Mori-Tanaka's theory in composite materials, Mechanics of Materials 6 (1987) 147–157. https://doi.org/10.1016/0167-6636(87)90005-6.

[55] J.D. Eshelby, The determination of the elastic field of an ellipsoidal inclusion, and related problems, Proc R Soc Lond A Math Phys Sci 241 (1957) 376–396. https://doi.org/10.1098/rspa.1957.0133.

[56] S.G. Abaimov, A.A. Khudyakova, S. V Lomov, On the closed form expression of the Mori–Tanaka theory prediction for the engineering constants of a unidirectional fiber-reinforced ply, Compos Struct 142 (2016) 1–6. https://doi.org/10.1016/j.compstruct.2016.02.001.

[57] Y. Luo, Iterative isotropization of the upper and lower bounds for accurate prediction of elastic properties of particulate composites, Results Phys 42 (2022) 106022.

[58] K. Lasn, A.T. Echtermeyer, A. Klauson, F. Chati, D. Décultot, Comparison of laminate stiffness as measured by three experimental methods, Polym Test 44 (2015) 143–152. https://doi.org/10.1016/j.polymertesting.2015.04.006.

[59] Test Method for Compressive Properties of Polymer Matrix Composite Materials with Unsupported Gage Section by Shear Loading, (2024). https://doi.org/10.1520/D3410_D3410M-16R24.

[60] Test Method for Shear Properties of Composite Materials by the V-Notched Beam Method, (2019). https://doi.org/10.1520/D5379_D5379M-19E01.

[61] Test Method for Shear Properties of Composite Materials by V-Notched Rail Shear Method, (2020). https://doi.org/10.1520/D7078_D7078M-20E01.

[62] Test Method for In-Plane Shear Response of Polymer Matrix Composite Materials by Tensile Test of a 45 Laminate, (2018). https://doi.org/10.1520/D3518_D3518M-18.

[63] Test Method for Compressive Properties of Unidirectional Polymer Matrix Composite Materials Using a Sandwich Beam, (2017). https://doi.org/10.1520/D5467_D5467M-97R17.

[64] Test Method for Flexural Properties of Polymer Matrix Composite Materials, (2021). https://doi.org/10.1520/D7264_D7264M-21.

[65] Test Method for Tensile Properties of Polymer Matrix Composite Materials, (2017). https://doi.org/10.1520/D3039_D3039M-17.

[66] L.A. Carlsson, D.F. Adams, R.B. Pipes, Basic experimental characterization of polymer matrix composite materials, Polymer Reviews 53 (2013) 277–302. https://doi.org/10.1080/15583724.2013.776588.

[67] L.A. Carlsson, D.F. Adams, R.B. Pipes, Experimental Characterization of Advanced Composite Materials: Fourth Edition (2014) 1–351. https://doi.org/10.1201/b16618.

[68] Emmanuel. Gdoutos, M.S.. Konsta-Gdoutos, Mechanical testing of materials, (2024) 294.

[69] M. El Messiry, S. Fathy, E. Eltahan, Comparative analysis of bending test methods for evaluating the stiffness of high-performance yarns, Journal of Engineered Fibers and Fabrics 20 (2025). https://doi.org/10.1177/15589250251329392.

[70] A. Wahjudi, A.S. Widodo, A comprehensive review on the non-destructive test for polymer matrix composite, Jurnal Rekayasa Mesin 14 (2023) 987–1000. https://doi.org/10.21776/JRM.V14I3.1681.

[71] F. Abdollahi-Mamoudan, C. Ibarra-Castanedo, X.P.V. Maldague, Non-Destructive Testing and Evaluation of Hybrid and Advanced Structures: A Comprehensive Review of Methods, Applications, and Emerging Trends, Sensors 25 (2025). https://doi.org/10.3390/S25123635.

[72] J.H. Tam, Z.C. Ong, Z. Ismail, B.C. Ang, S.Y. Khoo, Identification of material properties of composite materials using nondestructive vibrational evaluation approaches: A review, Mechanics of Advanced Materials and Structures 24 (2017) 971–986. https://doi.org/10.1080/15376494.2016.1196798.

[73] J. Jodhani, A. Handa, A. Gautam, Ashwni, R. Rana, Ultrasonic non-destructive evaluation of composites: A review, Mater Today Proc 78 (2023) 627–632. https://doi.org/10.1016/J.MATPR.2022.12.055.

[74] J.L. Rose, Successes and challenges in ultrasonic guided waves for NDT and SHM, Proceedings of the National Seminar & Exhibition on Non-Destructive Evaluation (2009). https://www.ndt.net/article/nde-india2009/pdf/1-PL-I.pdf (accessed July 14, 2025).

[75] J.E. Zimmer, J.R. Cost, Determination of the Elastic Constants of a Unidirectional Fiber Composite Using Ultrasonic Velocity Measurements, J Acoust Soc Am 47 (1970) 795–803. https://doi.org/10.1121/1.1911962.

[76] A. Castellano, P. Foti, A. Fraddosio, S. Marzano, M.D. Piccioni, Mechanical characterization of CFRP composites by ultrasonic immersion tests: Experimental and numerical approaches, Compos B Eng 66 (2014) 299–310. https://doi.org/10.1016/J.COMPOSITESB.2014.04.024.

[77] A. Castellano, P. Foti, A. Fraddosio, S. Marzano, M.D. Piccioni, Ultrasonic immersion tests for mechanical characterization of multilayered anisotropic materials, EESMS 2014 - 2014 IEEE Workshop on Environmental, Energy and Structural Monitoring Systems, Proceedings (2014) 63–68. https://doi.org/10.1109/EESMS.2014.6923266.

[78] T.T. Wu, Y.H. Liu, On the measurement of anisotropic elastic constants of fiber-reinforced composite plate using ultrasonic bulk wave and laser generated Lamb wave, Ultrasonics 37 (1999) 405–412. https://doi.org/10.1016/S0041-624X(99)00025-6.

[79] K. Lasn, A. Klauson, F. Chati, D. Décultot, Experimental determination of elastic constants of an orthotropic composite plate by using lamb waves, Mechanics of Composite Materials 47 (2011) 435–446. https://doi.org/10.1007/S11029-011-9221-Y.

[80] Y. Jiang, Y. Liu, J. Zeng, Y. Wang, Q. Xie, N. Hu, Equivalent elastic modulus measurement of cross-ply composite plates using Lamb waves, Compos Struct 321 (2023). https://doi.org/10.1016/J.COMPSTRUCT.2023.117230.

[81] A.L. Araújo, C.M. Mota Soares, M.J. Moreira De Freitas, Characterization of material parameters of composite plate specimens using optimization and experimental vibrational data, Compos B Eng 27 (1996) 185–191. https://doi.org/10.1016/1359-8368(95)00050-X.

[82] P.S. Frederiksen, Application of an improved model for the identification of material parameters, Mechanics of Composite Materials and Structures 4 (1997) 297–316. https://doi.org/10.1080/10759419708945886.

[83] P. Pedersen, P.S. Frederiksen, Identification of orthotropic material moduli by a combined experimental/numerical method, Measurement (Lond) (1992) 113–118.

[84] A.K. Bledzki, A. Kessler, R. Rikards, A. Chate, Determination of elastic constants of glass/epoxy unidirectional laminates by the vibration testing of plates, Compos Sci Technol 59 (1999) 2015–2024. https://doi.org/10.1016/S0266-3538(99)00059-7.

[85] D. Gsell, G. Feltrin, S. Schubert, R. Steiger, M. Motavalli, Cross-Laminated Timber Plates: Evaluation and Verification of Homogenized Elastic Properties, Journal of

Structural Engineering 133 (2007) 132–138. https://doi.org/10.1061/(ASCE)0733-9445(2007)133:1(132).

[86] R.F. Gibson, Modal vibration response measurements for characterization of composite materials and structures, Compos Sci Technol 60 (2000) 2769–2780. https://doi.org/10.1016/S0266-3538(00)00092-0.

[87] M.-J. Pindera, H. Khatam, A.S. Drago, Y. Bansal, Micromechanics of spatially uniform heterogeneous media: A critical review and emerging approaches, Compos B Eng 40 (2009) 349–378. https://doi.org/10.1016/j.compositesb.2009.03.007.

[88] Y. Zhong, L.Q.N. Tran, U. Kureemun, H.P. Lee, Prediction of the mechanical behavior of flax polypropylene composites based on multi-scale finite element analysis, J Mater Sci 52 (2017) 4957–4967. https://doi.org/10.1007/S10853-016-0733-7).

[89] F.L. Palombini, W. Kindlein, B.F. de Oliveira, J.E. de Araujo Mariath, Bionics and design: 3D microstructural characterization and numerical analysis of bamboo based on X-ray microtomography, Mater Charact 120 (2016) 357–368. https://doi.org/10.1016/J.MATCHAR.2016.09.022.

[90] M. Alhijazi, B. Safaei, Q. Zeeshan, M. Asmael, Modeling and simulation of the elastic properties of natural fiber-reinforced thermosets, Polym Compos 42 (2021) 3508–3517. https://doi.org/10.1002/pc.26075.

[91] A. Thuault, J. Bazin, S. Eve, J. Bréard, M. Gomina, Numerical study of the influence of structural and mechanical parameters on the tensile mechanical behaviour of flax fibres, Journal of Industrial Textiles 44 (2014) 22–39. https://doi.org/10.1177/1528083713481835.

[92] X. Xiong, S.Z. Shen, L. Hua, J.Z. Liu, X. Li, X. Wan, M. Miao, Finite element models of natural fibers and their composites: A review, Journal of Reinforced Plastics and Composites 37 (2018) 617–635. https://doi.org/10.1177/0731684418755552.

[93] E.J. Barbero, Introduction to composite materials design, 2nd ed., CRC Press, Boca Raton, FL, 2011.

[94] M. Nirbhay, A. Dixit, R.K. Misra, H.S. Mali, Tensile Test Simulation of CFRP Test Specimen Using Finite Elements, Procedia Materials Science 5 (2014) 267–273. https://doi.org/10.1016/J.MSPRO.2014.07.266.

[95] A. Hadăr, F. Baciu, A.-D. Voicu, D. Vlăsceanu, D.-I. Tudose, C. Adetu, Mechanical Characteristics Evaluation of a Single Ply and Multi-Ply Carbon Fiber-Reinforced Plastic Subjected to Tensile and Bending Loads, Polymers (Basel) 14 (2022). https://doi.org/10.3390/polym14153213.

[96] S. Badjie, Y.-F. Li, T.-H. Hsu, C.-H. Wu, Three-point bending test and finite-element analysis on frp bridge deck, in: 9th International Conference on Urban Earthquake Engineering/ 4th Asia Conference on Earthquake Engineering, Japan, 2012: pp. 1–7.

[97] E. Sabău, A. Trif, C.-Ş. Miron-Borzan, A. Popescu, Numerical Simulation of Flexural Behaviour of Glass Fiber Reinforced Polymer Composites, Academic Journal of Manufacturing Engineering (2021) 52.

[98] C. Dong, I.J. Davies, Flexural strength of bidirectional hybrid epoxy composites reinforced by e glass and T700S carbon fibres, Compos B Eng 72 (2015) 65–71. https://doi.org/10.1016/J.COMPOSITESB.2014.11.031.

[99] N. Kharghani, C. Guedes Soares, Experimental, numerical and analytical study of bending of rectangular composite laminates, European Journal of Mechanics, A/Solids 72 (2018) 155–174. https://doi.org/10.1016/J.EUROMECHSOL.2018.05.007.

[100] Y. Elmoghazy, E.M.O. Abuelgasim, S.A. Osman, Y.R.H. Afaneh, O.M.A. Eissa, B. Safaei, Effective Mechanical Properties Evaluation of Unidirectional and Bidirectional Composites Using Virtual Domain Approach at Microscale, Archives of Advanced Engineering Science 1 (2023) 27–37. https://doi.org/10.47852/BONVIEWAAES32021723.

[101] X. Deng, J. Hu, W.X. Wang, T. Matsubara, A micromechanical model for the analysis of multidirectional fiber reinforced polymer laminates, Compos Struct 208 (2019) 507–516. https://doi.org/10.1016/J.COMPSTRUCT.2018.10.019.

[102] C. González, J. LLorca, Mechanical behavior of unidirectional fiber-reinforced polymers under transverse compression: Microscopic mechanisms and modeling, Compos Sci Technol 67 (2007) 2795–2806. https://doi.org/10.1016/J.COMPSCITECH.2007.02.001.

[103] V. Kaushik, P. Sharma, P. Priyanka, H.S. Mali, Numerical modeling of fiber reinforced polymer textile composites for characterizing the mechanical behavior – a review, Materwiss Werksttech 53 (2022) 1263–1289.

[104] M. Smolnicki, G. Lesiuk, S. Duda, A.M.P. de Jesus, A Review on Finite-Element Simulation of Fibre Metal Laminates, Archives of Computational Methods in Engineering 30 (2023) 749–763. http://dx.doi.org/10.1007/s11831-022-09814-8.

[105] M. Smolnicki, P. Stabla, Finite element method analysis of fibre-metal laminates considering different approaches to material model, SN Appl Sci 1 (2019). https://doi.org/10.1007/S42452-019-0496-2.

[106] Q. Song, J. Xu, X. Chen, W. Huang, Y. Zeng, Z. Guo, Multiscale simulation and prediction of mechanical properties for carbon fiber reinforced polymer orthotropic laminate, Polym Compos 45 (2024) 7150–7163. https://doi.org/10.1002/pc.28256.

[107] N.K. Balasubramani, B. Zhang, N.T. Chowdhury, A. Mukkavilli, M. Suter, G.M. Pearce, Micro-mechanical analysis on random RVE size and shape in multiscale finite element modelling of unidirectional FRP composites, Compos Struct 282 (2022) 115081. https://doi.org/10.1016/j.compstruct.2021.115081.

[108] D. Trias, J. Costa, J.A. Mayugo, J.E. Hurtado, Random models versus periodic models for fibre reinforced composites, Comput Mater Sci 38 (2006) 316–324.

[109] L. Bouaoune, Y. Brunet, A. El Moumen, T. Kanit, H. Mazouz, Random versus periodic microstructures for elasticity of fibers reinforced composites, Compos B Eng 103 (2016) 68–73. https://doi.org/10.1016/J.COMPOSITESB.2016.08.026.

[110] J. Weng, W. Wen, H. Cui, B. Chen, Micromechanical analysis of composites with fibers distributed randomly over the transverse cross-section, Acta Astronaut 147 (2018) 133–140. https://doi.org/10.1016/J.ACTAASTRO.2018.03.056.

[111] M. Muthukumar, J. Prasath, Y.M. Desai, N.K. Naik, Mechanical behavior of unidirectional composites with hexagonal and uneven distribution of fibers in the transverse cross-section, J Compos Mater 52 (2018) 2985–3000. https://doi.org/10.1177/0021998318759742.

[112] K.K. Rumayshah, T. Dirgantara, H. Judawisastra, S. Wicaksono, Numerical micromechanics model of carbon fiber-reinforced composite using various periodical fiber arrangement, Journal of Mechanical Science and Technology 35 (2021) 1401–1406. https://doi.org/10.1007/S12206-021-0306-9.

[113] Y. Huang, K.K. Jin, S.K. Ha, Effects of fiber arrangement on mechanical behavior of unidirectional composites, J Compos Mater 42 (2008) 1851–1871. https://doi.org/10.1177/0021998308093910.

[114] G. Catalanotti, On the generation of RVE-based models of composites reinforced with long fibres or spherical particles, Compos Struct 138 (2016) 84–95. https://doi.org/10.1016/J.COMPSTRUCT.2015.11.039.

[115] B.C. Jin, A.A. Pelegri, Three-dimensional numerical simulation of random fiber composites with high aspect ratio and high volume fraction, J Eng Mater Technol 133 (2011). https://doi.org/10.1115/1.4004701.

[116] W. Tian, L. Xu, L. Qi, X. Chao, Minimum potential method appropriate to generate 2D RVEs of composites with high fiber volume fraction, Compos Struct 318 (2023). https://doi.org/10.1016/J.COMPSTRUCT.2023.117070.

[117] A.R. Melro, P.P. Camanho, S.T. Pinho, Generation of random distribution of fibres in long-fibre reinforced composites, Compos Sci Technol 68 (2008) 2092–2102. https://doi.org/10.1016/J.COMPSCITECH.2008.03.013.

[118] Z. Wang, X. Wang, J. Zhang, W. Liang, L. Zhou, Automatic generation of random distribution of fibers in long-fiber-reinforced composites and mesomechanical simulation, Mater Des 32 (2011) 885–891. https://doi.org/10.1016/J.MATDES.2010.07.002.

[119] Y. Hou, K. Zhang, Y. Lu, A. Noori, A new strategy for generating regional random fiber-reinforced polymer composite, Int J Mech Sci 251 (2023). https://doi.org/10.1016/J.IJMECSCI.2023.108346.

[120] R. Nakka, D. Harursampath, M. Pathan, S.A. Ponnusami, A computationally efficient approach for generating RVEs of various inclusion/fibre shapes, Compos Struct 291 (2022). https://doi.org/10.1016/J.COMPSTRUCT.2022.115560.

[121] Y. Ismail, D. Yang, J. Ye, Discrete element method for generating random fibre distributions in micromechanical models of fibre reinforced composite laminates, Compos B Eng 90 (2016) 485–492. https://doi.org/10.1016/J.COMPOSITESB.2016.01.037.

[122] L. Yang, Y. Yan, Z. Ran, Y. Liu, A new method for generating random fibre distributions for fibre reinforced composites, Compos Sci Technol 76 (2013) 14–20. https://doi.org/10.1016/J.COMPSCITECH.2012.12.001.

[123] T. Zhang, Y. Yan, A comparison between random model and periodic model for fiber-reinforced composites based on a new method for generating fiber distributions, Polym Compos 38 (2017) 77–86. https://doi.org/10.1002/PC.23562.

[124] A. Bahmani, G. Li, T.L. Willett, J. Montesano, Three-dimensional microscopic assessment of randomly distributed representative volume elements for high fiber volume fraction unidirectional composites, Compos Struct 192 (2018) 153–164. https://doi.org/10.1016/J.COMPSTRUCT.2018.02.075.

[125] I.M. Gitman, H. Askes, L.J. Sluys, Representative volume: Existence and size determination, Eng Fract Mech 74 (2007) 2518–2534. https://doi.org/10.1016/J.ENGFRACMECH.2006.12.021.

[126] T. Kanit, S. Forest, I. Galliet, V. Mounoury, D. Jeulin, Determination of the size of the representative volume element for random composites: Statistical and numerical approach, Int J Solids Struct 40 (2003) 3647–3679. https://doi.org/10.1016/S0020-7683(03)00143-4.

[127] H. Bisheh, Uncertainty analysis for prediction of elastic properties of unidirectional bamboo fiber-reinforced composites, Structures 54 (2023) 198–220. https://doi.org/10.1016/J.ISTRUC.2023.05.032.

[128] S. Koley, P.M. Mohite, C.S. Upadhyay, A micromechanical study of fibre-reinforced composites with uncertainty quantification and statically equivalent random fibre distribution, Lecture Notes in Mechanical Engineering (2019) 37–48. https://doi.org/10.1007/978-981-15-1189-9_4.

[129] Y. Luo, A Numerical Comparison between Geometry and Voxel Based Finite Element Modeling for Elasticity Characterization of Particulate Composites, International Journal of Composite Materials 11 (2021) 54–61. https://doi.org/10.5923/j.cmaterials.20211103.02.

[130] K. Hole, Finite element mesh generation methods: a review and classification, Comput Aided Des 20 (1988) 27–38.

[131] S.H. Lo, Finite element mesh generation and adaptive meshing, Progress in Structural Engineering and Materials 4 (2002) 381–399.

[132] A. Doitrand, C. Fagiano, F.X. Irisarri, M. Hirsekorn, Comparison between voxel and consistent meso-scale models of woven composites, Compos Part A Appl Sci Manuf 73 (2015) 143–154. https://doi.org/10.1016/j.compositesa.2015.02.022.

[133] A. Sas, N. Ohs, E. Tanck, G.H. van Lenthe, Nonlinear voxel-based finite element model for strength assessment of healthy and metastatic proximal femurs, Bone Rep 12 (2020) 100263. https://doi.org/10.1016/j.bonr.2020.100263.

[134] L. Gulfo, O. Haglund Nilsson, J. Sjöberg, I. Katsivalis, L.E. Asp, M. Fagerström, A 3D voxel-based mesostructure generator for finite element modelling of tow-based discontinuous composites, Compos B Eng 278 (2024) 111405-. https://doi.org/10.1016/j.compositesb.2024.111405.

[135] J. Ryatt, M. Ramulu, Numerical investigation of the application of voxel based meshes for stochastic tow based discontinuous composites, Finite Elements in Analysis and Design 214 (2023). https://doi.org/10.1016/J.FINEL.2022.103874.

[136] J. Ryatt, M. Ramulu, Prediction of tensile failure of stochastic tow-based discontinuous composites via mesoscale finite element analysis, Compos Struct 279 (2022). https://doi.org/10.1016/J.COMPSTRUCT.2021.114769.

[137] J. Schneider, G. Hello, Z. Aboura, D. Marsal, A meso-FE voxel model of an interlock woven composite, in: Proceeding of the International Conference in Composite Materials 17th (ICCM17), Edinburgh, Scotland, 2009. https://www.researchgate.net/publication/267992407 (accessed July 24, 2025).

[138] D. Zhang, A.M. Waas, A micromechanics based multiscale model for nonlinear composites, Acta Mech 225 (2014) 1391–1417. https://doi.org/10.1007/s00707-013-1057-1.

[139] Jacob. Aboudi, S.M.. Arnold, B.A.. Bednarcyk, Micromechanics of composite materials : a generalized multiscale analysis approach, Elsevier, 2013.

[140] A.A. Gusev, P.J. Hine, I.M. Ward, Fiber packing and elastic properties of a transversely random unidirectional glass/epoxy composite, Compos Sci Technol 60 (2000) 535–541.

[141] Y. Luo, Microstructure-free finite element modeling for elasticity characterization and design of fine-particulate composites, Journal of Composites Science 6 (2022) 35.

[142] Y. Luo, An Accuracy Comparison of Micromechanics Models of Particulate Composites against Microstructure-Free Finite Element Modeling, Materials 15 (2022) 4021.

[143] S.W. Tsai, H.T. Hahn, Introduction to composite materials, 1980.

[144] D. Hull, T.W. Clyne, An introduction to composite materials, 2012.

[145] R. Younes, A. Hallal, F. Fardoun, F. Hajj, Comparative Review Study on Elastic Properties Modeling for Unidirectional Composite Materials, Composites and Their Properties (2012). https://doi.org/10.5772/50362.

[146] A.E. Krauklis, A.I. Gagani, A.T. Echtermeyer, Hygrothermal Aging of Amine Epoxy: Reversible Static and Fatigue Properties, Open Engineering (Warsaw) 8 (2018) 447–454. https://doi.org/10.1515/eng-2018-0050.

[147] Z.-M. Huang, Y.-X. Zhou, Strength of Fibrous Composites, 1. Aufl., Springer-Verlag, Berlin, Heidelberg, 2011.

[148] A. Cherkaev, Variational Methods for Structural Optimization, 140 (2000). https://doi.org/10.1007/978-1-4612-1188-4.

[149] G.W. Milton, The Theory of Composites, The Theory of Composites (2002). https://doi.org/10.1017/CBO9780511613357.

[150] V. Mityushev, R. Kycia, W. Nawalaniec, N. Rylko, Introduction to mathematical modeling and computer simulations: Second edition, Introduction to Mathematical Modeling and Computer Simulations: Second Edition (2024) 1–330. https://doi.org/10.1201/9781032684284.